Publication Year	2020
Acceptance in OA@INAF	2021-09-03T14:20:35Z
Title	Measuring HERA's Primary Beam in Situ: Methodology and First Results
Authors	Nunhokee, CD; Parsons, AR; Kern, NS; Nikolic, B; Pober, JC; et al.
DOI	10.3847/1538-4357/ab9634
Handle	http://hdl.handle.net/20.500.12386/31040
Journal	THE ASTROPHYSICAL JOURNAL
Number	897

The Astrophysical Journal, 897:5 (17pp), 2020 July 1 https://doi.org/10.3847/1538-4357/ab9634
© 2020. The American Astronomical Society. All rights reserved.

Measuring HERA's Primary Beam in Situ: Methodology and First Results

Chuneeta D. Nunhokee[1], Aaron R. Parsons[1], Nicholas S. Kern[1], Bojan Nikolic[2], Jonathan C. Pober[3], Gianni Bernardi[4,5,6], Chris L. Carilli[7], Zara Abdurashidova[1], James E. Aguirre[8], Paul Alexander[2], Zaki S. Ali[1], Yanga Balfour[6], Adam P. Beardsley[9], Tashalee S. Billings[8], Judd D. Bowman[9], Richard F. Bradley[10], Jacob Burba[3], Carina Cheng[1], David R. DeBoer[1], Matt Dexter[1], Eloy de Lera Acedo[2], Joshua S. Dillon[1], Aaron Ewall-Wice[11], Nicolas Fagnoni[2], Randall Fritz[12], Steve R. Furlanetto[13], Kingsley Gale-Sides[2], Brian Glendenning[7], Deepthi Gorthi[1], Bradley Greig[14,15], Jasper Grobbelaar[12], Ziyaad Halday[12], Bryna J. Hazelton[16,17], Jacqueline N. Hewitt[11], Daniel C. Jacobs[9], Austin Julius[12], Joshua Kerrigan[3], Piyanat Kittiwisit[9], Saul A. Kohn[8], Matthew Kolopanis[9], Adam Lanman[3], Paul La Plante[8], Telalo Lekalake[12], Adrian Liu[1,18,21], David MacMahon[1], Lourence Malan[12], Cresshim Malgas[12], Matthys Maree[12], Zachary E. Martinot[8], Eunice Matsetela[12], Andrei Mesinger[19], Mathakane Molewa[12], Miguel F. Morales[16], Tshegofalang Mosiane[12], Abraham R. Neben[11], Nipanjana Patra[1], Samantha Pieterse[12], Nima Razavi-Ghods[2], Jon Ringuette[16], James Robnett[7], Kathryn Rosie[12], Peter Sims[3], Craig Smith[12], Angelo Syce[12], Nithyanandan Thyagarajan[7,9,22], Peter K. G. Williams[20], and Haoxuan Zheng[11]

[1] Department of Astronomy, University of California, Berkeley, CA, USA; cnunhokee@berkeley.edu
[2] Cavendish Astrophysics, University of Cambridge, Cambridge, UK
[3] Department of Physics, Brown University, Providence, RI, USA
[4] INAF-Istituto di Radioastronomia, via Gobetti 101, I-40129 Bologna, Italy
[5] Department of Physics and Electronics, Rhodes University, P.O. Box 94, Grahamstown, 6140, South Africa
[6] South African Radio Astronomy Observatory, Black River Park, 2 Fir Street, Observatory, Cape Town, 7925, South Africa
[7] National Radio Astronomy Observatory, Socorro, NM, USA
[8] Department of Physics and Astronomy, University of Pennsylvania, Philadelphia, PA, USA
[9] School of Earth and Space Exploration, Arizona State University, Tempe, AZ, USA
[10] National Radio Astronomy Observatory, Charlottesville, VA, USA
[11] Department of Physics, Massachusetts Institute of Technology, Cambridge, MA, USA
[12] SKA-SA, Cape Town, South Africa
[13] Department of Physics and Astronomy, University of California, Los Angeles, CA, USA
[14] School of Physics, University of Melbourne, Parkville, VIC 3010, Australia
[15] ARC Centre of Excellence for All-Sky Astrophysics in 3 Dimensions (ASTRO 3D), Australia
[16] Department of Physics, University of Washington, Seattle, WA, USA
[17] eScience Institute, University of Washington, Seattle, WA, USA
[18] Department of Physics and McGill Space Institute, McGill University, 3600 University Street, Montreal, QC H3A 2T8, Canada
[19] Scuola Normale Superiore, I-56126 Pisa, PI, Italy
[20] Harvard-Smithsonian Center for Astrophysics, Cambridge, MA, USA
Received 2019 October 7; revised 2020 May 22; accepted 2020 May 23; published 2020 June 26

Abstract

The central challenge in 21 cm cosmology is isolating the cosmological signal from bright foregrounds. Many separation techniques rely on the accurate knowledge of the sky and the instrumental response, including the antenna primary beam. For drift-scan telescopes, such as the Hydrogen Epoch of Reionization Array (HERA), that do not move, primary beam characterization is particularly challenging because standard beam-calibration routines do not apply (Cornwell et al.) and current techniques require accurate source catalogs at the telescope resolution. We present an extension of the method from Pober et al. where they use beam symmetries to create a network of overlapping source tracks that break the degeneracy between source flux density and beam response and allow their simultaneous estimation. We fit the beam response of our instrument using early HERA observations and find that our results agree well with electromagnetic simulations down to a −20 dB level in power relative to peak gain for sources with high signal-to-noise ratio. In addition, we construct a source catalog with 90 sources down to a flux density of 1.4 Jy at 151 MHz.

Unified Astronomy Thesaurus concepts: Cosmology (343); H I line emission (690); Radio astronomy (1338)

1. Introduction

The 21 cm line from neutral hydrogen (H I line) has gained attention as a probe of structure formation in the early universe. Low-frequency observations probe high redshifts and therefore hold the potential to explore different epochs in the history of the universe. Using the 21 cm H I line, we can study the Cosmic Dawn, when the first luminous sources such as Population III stars and massive X-ray sources formed (Furlanetto 2016; McQuinn 2016), and the Epoch of Reionization (EoR), when these first luminous sources emitted ultraviolet and/or X-ray radiations and ionized the neutral intergalactic medium (IGM) over $z \sim 15$–6 (Ciardi & Ferrara 2005; Zaroubi 2013). At closer redshifts, observations of the 21 cm line help probe the baryonic acoustic oscillations (BAO) which serve as tracers of the expansion of the universe, allowing the study of the evolution of dark energy (Bandura et al. 2014; Newburgh et al. 2016).

Considerable effort is being dedicated toward measuring highly redshifted 21 cm fluctuations. Active experiments

[21] Hubble Fellow.
[22] Jansky Fellow of the National Radio Astronomy Observatory.

include the Precision Array to Probe the Epoch of Reionization (PAPER; Parsons et al. 2010), the Giant Metrewave Radio Telescope Epoch of Reionization (GMRT; Paciga et al. 2011), the Murchison Widefield Array (MWA; Tingay et al. 2013), the LOw Frequency Array (LOFAR; van Haarlem et al. 2013), the Canadian Hydrogen Intensity Mapping Experiment (CHIME; Bandura et al. 2014), the Square Kilometer Array (SKA; Koopmans et al. 2015), the Hydrogen Intensity and Real-time Analysis eXperiment (HIRAX; Newburgh et al. 2016), and HERA (DeBoer et al. 2017).

Observations of the 21 cm signal require the separation of astrophysical foregrounds that are ∼4–5 orders of magnitude brighter than the cosmological signal. Current foreground mitigation techniques have two flavors: foreground subtraction (or removal) and avoidance. Both techniques rely on the different spectral behavior of the foreground and the expected 21 cm emission. Subtraction methods attempt to model and subtract foreground emission from the observations (Morales et al. 2006; Bowman et al. 2009; Liu et al. 2009; Bernardi et al. 2010, 2013; Chapman et al. 2016), while the avoidance approach exploits how foregrounds are confined to a wedge-shaped region in the Fourier space to reveal an "EoR window" where the foreground contamination is minimal with respect to the 21 cm signal (Morales & Hewitt 2004; Vedantham et al. 2012; Pober et al. 2013; Liu et al. 2014a, 2014b; Thyagarajan et al. 2015a).

Recently, Kerrigan et al. (2018) showed that foreground modeling helps reduce foreground power in the wedge, mitigating its possible spillover into the EoR window. However, the efficiency of the subtraction method depends on accurate sky and instrument models: variable primary beams contribute to modeling errors, particularly for wide-field observations. Though these errors can, in principle, be mitigated through calibration (Mitchell et al. 2008; Bernardi et al. 2010, 2013; Yatawatta et al. 2013), improper modeling can lead to additional errors that are significant enough to contaminate the cosmological signal (Thyagarajan et al. 2015a, 2015b; Nunhokee et al. 2017; Procopio et al. 2017).

Electromagnetic (EM) simulations are used to model primary beam responses; however, they fall short in including subtle real-world effects such as feed misalignment, antenna-to-antenna variation, and cross-coupling between neighboring antennas. Unfortunately, inaccurate beam models may lead to spurious spectral structures, improper scaling in the calibration solutions, and inaccurate power spectra normalization. Hence, we need techniques to characterize the instrument response using drift-scan wide-field observations and validate outputs of the EM simulations.

Measurements of the primary beam is a requirement for both single-dish radio telescopes and radio interferometers. Substantial efforts have been dedicated toward characterizing the primary beam of an antenna lately. For example, Neben et al. (2016) and Line et al. (2018) use the ORBCOMM satellite to map the antenna response. Holography, a well-known technique in radio astronomy, is also used to study the instrument response (Berger et al. 2016). Recently, Virone et al. (2014), Pupillo et al. (2015), Jacobs et al. (2017), and de Lera Acedo et al. (2018) have demonstrated that we can make direct measurements of the primary beam using unmanned aerial vehicles; however, they are accompanied by challenges that require further investigation. Our work describes a technique for measuring the instrument response using drift-scan wide-field observations similar to Pober et al. (2012) and Eastwood et al. (2018).

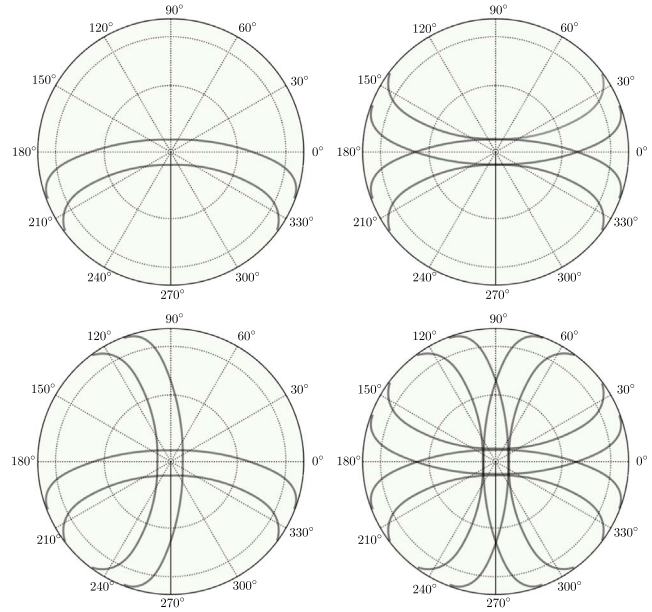

Figure 1. Top left: a schematic representation of two arbitrary source tracks crossing the primary beam of our instrument. Top right: source tracks overlaid with the corresponding 180° mirrored tracks. Bottom left: source tracks overlaid with the corresponding 90° rotated tracks. Bottom right: source tracks overlaid with a combination of 180° mirrored tracks, and 90° and 270° rotated tracks. The projection is orthographic with the center indicating zenith and the dotted lines are spaced 30°.

This paper is organized as follows: the formalism is derived in Section 2, the observations and data processing are described in Section 3, and the results are discussed in Sections 4 and 5. We show the effects of confusion noise in Section 6 and conclude in Section 7.

2. Formalism

A zenith-pointing telescope operating in drift-scan mode observes the radio sky as it passes across the primary beam of the instrument, placing astronomical sources at different points in the beam. The measured or apparent flux density of a source I'_ν at any given time t and frequency ν can be related to its intrinsic flux density I_ν as follows:

$$I'_\nu(\hat{s}, t) = A_\nu(\hat{s}, t) I_\nu(\hat{s}) + n(\hat{s}, t), \tag{1}$$

where A_ν is the primary beam response in the direction of the source $\hat{s}$ and time t as sources pass through different beam responses at different times. Each measurement is associated with a noise denoted by $n(\hat{s}, t)$. Examples of two arbitrary sources being traced are shown in the top-left panel of Figure 1. If we know the intrinsic flux densities of these two sources, it is trivial to evaluate the primary beam values at these source locations using Equation (1). Multiple sources then enable us to obtain full coverage of the instrument response.

However, precise measurements of the flux densities or catalogs consistent with the resolution of the observing telescope are often limited. We therefore simultaneously solve for $A_\nu(\hat{s}, t)$ and $I_\nu(\hat{s})$ in Equation (1). We use a nonlinear least-squares optimization as it has the ability to linearize the function and iteratively solves for the unknowns until convergence is achieved. Nevertheless, sources with different

declinations transit through different parts of the primary beam, rendering the beam solutions degenerate with flux densities of the sources. We overcome this problem by introducing beam symmetries that break the degeneracy between the beam response and flux density. Following this approach, each source forms two or more tracks: the actual and the rotated/mirrored ones. Examples of beam symmetries are the 180° mirror symmetry (top right, Figure 1) and 90° rotation (bottom left, Figure 1) about the source tracks. We can include multiple beam symmetries, for example, a combination of the 180° mirror symmetry, and the 90° and 270° rotations about the source tracks, as shown in the bottom-right panel of Figure 1. These overlapping source tracks relate to the flux densities of sources at different declinations.

2.1. Forming the Least-squares Problem

We use an $n \times n$ grid to represent the empirical primary beam. Each grid pixel represents the sine projection of the azimuth–altitude angles (ϕ, θ). The pixel resolution is estimated from the sampling such that each grid pixel within the field of view (FoV) has at least one datum. It must be small enough to preserve our assumption that the source tracks share the same beam response when they cross each other. To increase the signal-to-noise ratio (S/N), we represent the primary beam value at any given source location and time using a linear interpolation of the four closest pixels.

Now that we have our gridded measurements and a network of overlapping source tracks using the beam symmetries, we form a least-squares optimization problem. For any given source $\hat{s}$, we aim to minimize

$$\min \sum_{t,\hat{s}} |I'_\nu(\hat{s}, t) - A_\nu(\hat{s}, t) I_\nu(\hat{s})|^2 = \min \sum_{t,\hat{s}} \left| I'_\nu(\hat{s}, t) - \sum_{k=0}^{4} a_k(\hat{s}, t) \frac{1}{d_k} I_\nu(\hat{s}) \right|^2, \quad (2)$$

where the summation over k represents the linear interpolation between the four closest pixels with a_k denoting the beam solution at grid index k. Each grid index k is mapped to a (ϕ, θ) on the 2D grid. The distance d_k is calculated with respect to the azimuth–altitude angle (ϕ_0, θ_0) evaluated at source $\hat{s}$ and time t.

With multiple sources, we can construct a solvable matrix in the form

$$\boldsymbol{m} = \boldsymbol{C}\hat{\boldsymbol{x}} + \hat{\boldsymbol{n}}, \quad (3)$$

where $\boldsymbol{m}$ is the vector of measurements containing values for $I'_\nu(\hat{s}, t)$, $\boldsymbol{C}$ is the condition matrix describing the combination and conditions of the parameters, and $\hat{\boldsymbol{x}}$ contains the unknown parameters: beam response a_k and source flux density $I_\nu(\hat{s})$.

Given that the system shown in Equation (3) comprises two unknowns parameters, it is nonlinear; hence we use the Gauss–Newton algorithm to solve for a_k and $I_\nu(\hat{s})$. This algorithm is second-order iterative whose convergence is dependent on the initial guesses of the unknown parameters. At each iteration, the equation is expressed as a Taylor expansion about the solutions derived in the previous iteration using the `linsolve`[23] package.

[23] https://github.com/HERA-Team/linsolve

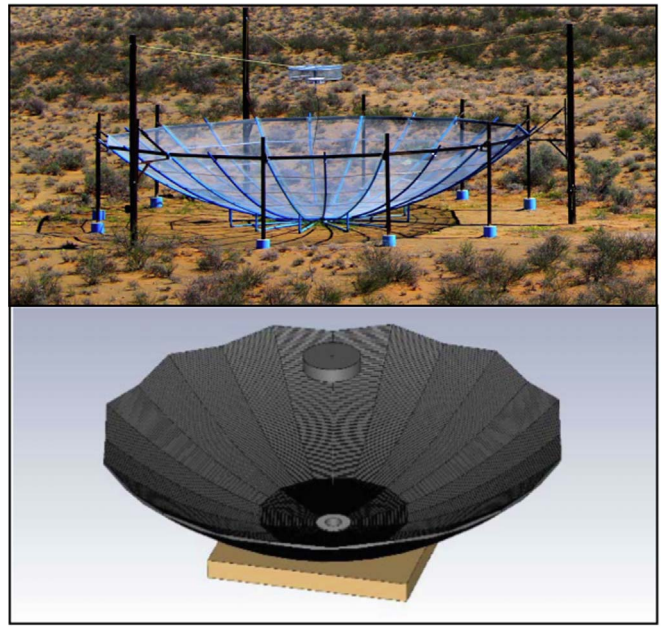

Figure 2. Top: a HERA dish with a crossed-dipole feed as installed at Karoo desert in South Africa. Bottom: a 14 m dish and a crossed-dipole feed model generated using CST for EM simulations.

2.2. Using Prior Knowledge of the Sky

As mentioned in Section 2.1, we need to provide initial guesses for a better convergence in Equation (2). Estimates of $I_\nu(\hat{s})$ are calculated using

$$I_\nu(\hat{s}) = \frac{\sum_t w_\nu(\hat{s}, t) I'_\nu(\hat{s}, t)}{\sum_t w_\nu(\hat{s}, t) A_\nu^{\mathrm{M}}(\hat{s}, t)}, \quad (4)$$

where $A_\nu^{\mathrm{M}}(\hat{s}, t)$ is the primary beam value evaluated from EM simulations at source $\hat{s}$, time t, and frequency ν, and w_ν are the weights assigned to the measurements I'_ν. In our case, we take w_ν to be $A_\nu^{\mathrm{M}}(\hat{s}, t)$. Given that I'_ν are already weighted by the instrument's primary beam, this additional weighting accounts for the time samples averaged into each beam pixel, thus, providing an effective approximation of the inverse-variance weighting (Jacobs et al. 2013).

2.3. Electromagnetic Simulations

The beam models used in this work are generated using the Computer Simulation Technology (CST) software (Fagnoni et al. 2019). The antenna setup used for the simulation is illustrated in Figure 2. The dish is a 14 m diameter paraboloid made up of an aluminum mesh held by a framework of PVC pipes converging into a cylindrical concrete slab at the center of the dish. The crossed-dipole feed (previously used for PAPER) is enclosed in a cylindrical cage. It is sensitive to east–west and north–south polarizations, and is sandwiched between two steel disks that act as sleeves to broaden the frequency response by creating a dual-resonance structure (Parsons et al. 2010).

The simulation accounts for the EM properties of different materials in use, including conductivity of metals, dielectrics of the propagation medium, and signal attenuation (Fagnoni et al. 2019). However, they do not include certain real-world effects such as uneven ground plane and feed misalignment. Fagnoni et al. (2019) produce beam models both with and without the effects of mutual coupling. We use the EM simulations without

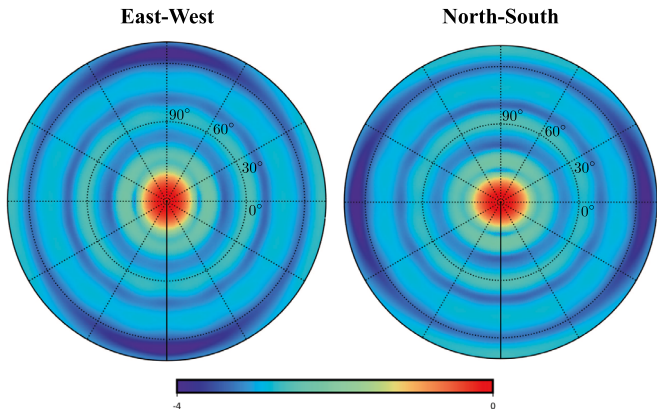

Figure 3. Primary beam models generated by the EM simulation in the east–west (left) and north–south (right) polarizations.

mutual coupling. The resulting primary beam models for the east–west and north–south polarizations can be seen in Figure 3. The beam model in the east–west polarization is assumed to be a 90° rotation of the north–south polarization.

3. Observation

The measurements used in this paper are taken from the HERA Phase I configuration, comprising 52 antennas (Figure 4) that reach out to a *uv* distance of 75λ as illustrated in Figure 5. Details of the observational setup are listed in Table 1.

3.1. Data Reduction and Calibration

We use data from the Second Internal Data Release (IDR2) processed with the HERA analysis and reduction pipeline, which are flagged for faulty antennas and radio frequency interference (RFI) (Kerrigan et al. 2019; A. Beardsley 2020, in preparation).

The HERA layout is such that we can employ redundant calibration, a powerful technique that uses the property of redundant baselines measuring the same sky signal (Liu et al. 2010; Zheng 2014; Dillon & Parsons 2016; Dillon et al. 2020). Redundant calibration iteratively solves for the per-antenna, per-time, and per-frequency instrumental complex gains by minimizing the sum of the deviations of the per-baseline measured visibilities V'_{ij} from that of the model $V_{ij}(t, \nu)$ such that

$$\min \sum_{bl} \frac{|V'_{ij} - g_i g_j^* V_{ij}(t, \nu)|^2}{\sigma_{ij}^2}, \tag{5}$$

where g_i and g_j are the complex antenna gains for antennas i and j respectively, and σ_{ij}^2 is the noise in the per-baseline measured visibilities. The sum is taken over all the redundant baselines denoted by bl. The model visibilities V_{ij} are initially taken as the averaged visibilities of the redundant baselines and are updated at each iteration.

However, the overall amplitude and phase of the complex gain solutions obtained from Equation (5) remain unknown. In order to correct for these overall amplitude and phase degeneracies, the data must be tied to a model of the sky (Dillon et al. 2018). In the HERA Phase I reduction pipeline, this is done using bright sources from the GLEAM catalog (Hurley-Walker et al. 2017) in conjunction with the EM simulations without mutual coupling (Fagnoni et al. 2019) to create a set of model visibilities that is used to solve for direction-independent antenna-based gains for a single field (Kern et al. 2020), achieved using standard routines in the Common Astronomy Software Applications (CASA) package. This calibration is applied to one night of good data, which

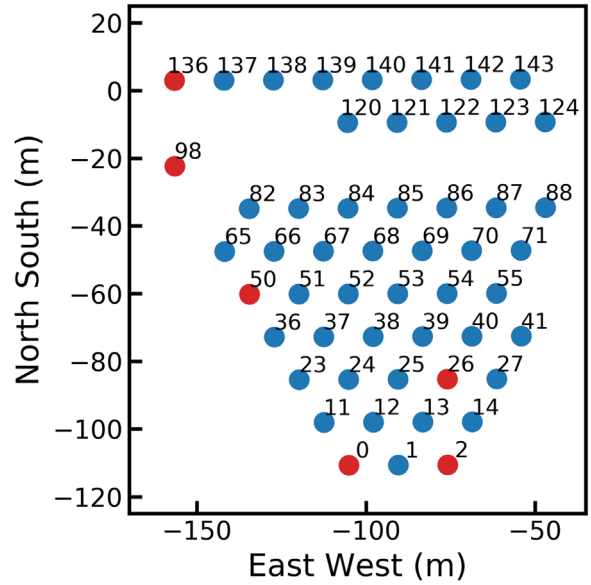

Figure 4. HERA 52 antenna configuration. Malfunctioning elements highlighted in red for 2018 December 24, 25, and 26 were not included in this work.

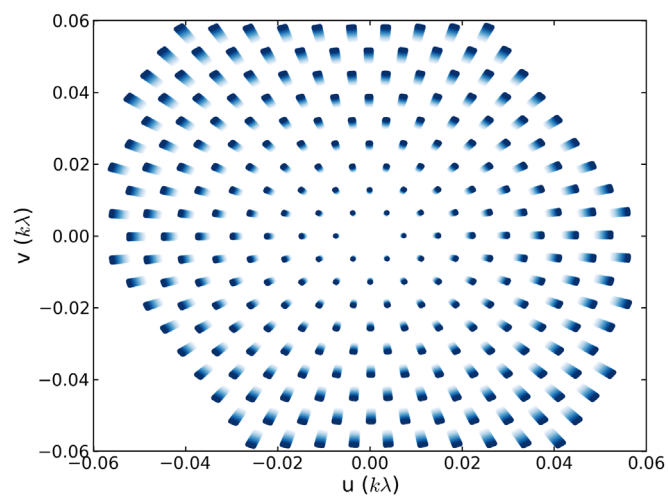

Figure 5. UV sampling generated from the antenna configuration for a 10 MHz frequency band centered at 150 MHz. The transition in color from faint to bright represents the variation of the *uv* sampling as a function of increasing frequency. Note the change in amplitude as sources cross through the primary beam.

Table 1
Summary of HERA Phase I Setup

Array longitude	21°25′41.″9
Array latitude	−30°43′17.″5
Number of dishes	52
Frequency range	100–200 MHz
Number of channels	1024
Integration time	10.7 s
Daily Observing time	6 pm to 6 am SAST
Daily Observing duration	12 hr
Observing days	Decl. 24, 25, 26, 2018

themselves then become the model visibilities for calibrating other nights in the data release. For more details on redundant and absolute calibration in the HERA reduction pipeline, we refer the reader to Dillon et al. (2020) and Kern et al. (2020), respectively.

3.2. Imaging

Radio interferometers propagate voltages from each antenna to a correlator where the inputs are cross multiplied and time averaged. These cross-correlated measurements, termed as visibilities, are Fourier transforms of the radio emission from the sky under a flat-sky approximation. Hence, to image the sky, we need to Fourier-transform the data back to the image domain. The operation is not straightforward as the measured visibilities are now convolved with the instrument response. Assuming a flat sky, the resulting sky image $I^D(l, m, \nu)$ can be obtained using (Thompson et al. 2017)

$$A(l, m, \nu)I^D(l, m, \nu) = \iint S(u, v)V^c \times (u, v, \nu)e^{2\pi i(ul+vm)}\, dudv, \quad (6)$$

where $V^c(u, v)$ denotes the calibrated visibilities (refer to Section 3.1), $S(u, v)$ represents the sampling function (also known as the uv coverage; Figure 5)), and (l, m) are the direction cosines relative to the source position. The resulting image I^D is generally known as "the dirty image" as it is the sky signal convolved with the point-spread function (Fourier transform of the sampling function).

Wide-field imaging is limited by various factors including bandwidth and time smearing, and non-coplanar baselines (Cornwell et al. 2005). While forming images, we need to choose the time interval and bandwidth over which we can assume constant source emission to prevent radial smearing. Single-channel imaging is ideal; however, given the poor uv coverage of our instrument we need to find an optimal frequency interval with minimum bandwidth smearing. This optimal frequency band $\Delta\nu$ is dependent on the resolution of the instrument such that (McMullin et al. 2007)

$$\Delta\nu < \nu_0 \left(\frac{D}{b_{\max}}\right), \quad (7)$$

where $b_{\max}$ is the maximum baseline length, D is the dish diameter, and ν_0 is the reference frequency (taken as the center frequency in our case). We find that assuming constant source emission over a 10 MHz band and 10 minute interval provides us with the minimum smearing along time and frequency axes.

To form images, we use a sampling of $\Delta l \approx 1/2u_{\max} \approx 8'$ and $\Delta m \approx 1/2v_{\max} \approx 8'$ and the multifrequency synthesis (MFS) algorithm embedded in the CASA package. The MFS algorithm combines data from all the frequency channels within the specified band onto a single spatial-frequency grid, assuming a constant sky brightness throughout. This assumption can cause spurious spatial structures for sources with spectral variations and high dynamic ranges. Because our current observations are looking at a dynamic range of a few hundreds, the basic MFS algorithm is sufficient.

Another limitation of wide-field imaging is that the standard assumption of a nonzero w term in interferometric imaging (Equation (6)) no longer applies and hence sources that are away from the zenith may be distorted or may introduce artifacts (Cornwell et al. 2005). We use the w-projection algorithm in CASA to correct for the w terms. We choose 128 w projections based on HERA's FoV, which is about 20°.

Furthermore, the images are formed using baselines greater than 30 m to reduce contaminations from diffuse emission. The data are then uniformly gridded onto the uv plane, boosting image pixels with low weights, thus allowing for a sharp resolution and side-lobe reduction in the FoV. Each grid pixel is weighted by the inverse of the number of visibilities that fall within the grid. As the generated images are convolved with the point-spread function (also known as the "dirty beam"), we use the iterative Cotton–Schwab deconvolution algorithm (Cornwell et al. 2005), embedded in CASA to isolate the sky image from the point-spread function. The cleaning mask is set to the FWHM of the primary beam and cleans down to the first negative clean component. Deconvolved images centered at 130 MHz (top panel) and 150 MHz (bottom panel) are shown in Figure 6. They comprise mostly point sources, and the dynamic range is ∼1:30. The size of these point sources decreases as a function of increasing frequency as a result of variation in the point-spread function. The flux density decreases as well with increasing frequency as extragalactic sources emit synchrotron emission.

3.3. Source Extraction

Once we have the deconvolved images as described in Section 3.2, we run the source finder software Python Blob Detection and Source Finder (PyBDSF; Mohan & Rafferty 2015) to find potential point sources. The finder identifies source candidates in islands of pixels brighter than 1 Jy. This choice of threshold is estimated using the rms across pixels in the images generated at different local sidereal times (LST). We fit a Gaussian to the pixel intensity distribution and calculate the standard deviation. Figure 7 shows the confusion noise as a function of the LST. We notice that the confusion noise peaks when a bright source is in or near the FoV; for instance, we have Fornax A, Pictor A, Virgo A, and Centaurus A transiting at LST 3, 5, 12, and 13 hr, respectively. The average rms across LSTs is about ∼0.18 Jy; hence ,we set the PyBDSF threshold to be five times the rms value, identifying sources above 1 Jy.

Because each image spans a 10 minute observation and the beam-crossing timescale is 10 minutes, the sources can be found in different images, possibly with different centered peaks. We overcome this issue by averaging all sources within 1′, resulting in 113 unique sources including Fornax A. The decl. range of these sources is limited within HERA's FoV between −20° and −40° while the R.A. spans the duration of the observation which is 12 hr.

We then compare our extracted source candidates with the GLEAM survey (Hurley-Walker et al. 2017). We find counterparts for 90 of the sources, plotted in Figure 8. Most of the extracted positions match with the GLEAM results within 10%–20% except for a few sources for which the difference goes up to 30% (refer to Section 5 for a detailed explanation). The remaining 23 sources include Fornax A (red star; Figure 8)) and sources located within the Magellanic Clouds (blue crosses; Figure 8)) that are excluded in the GLEAM survey.

We produce a mosaic (Figure 9) using the individual snapshots to illustrate the sky seen by HERA at 150 MHz during a night of observation. The mosaic is constructed using Equation (4), hence it shows estimates of the intrinsic flux

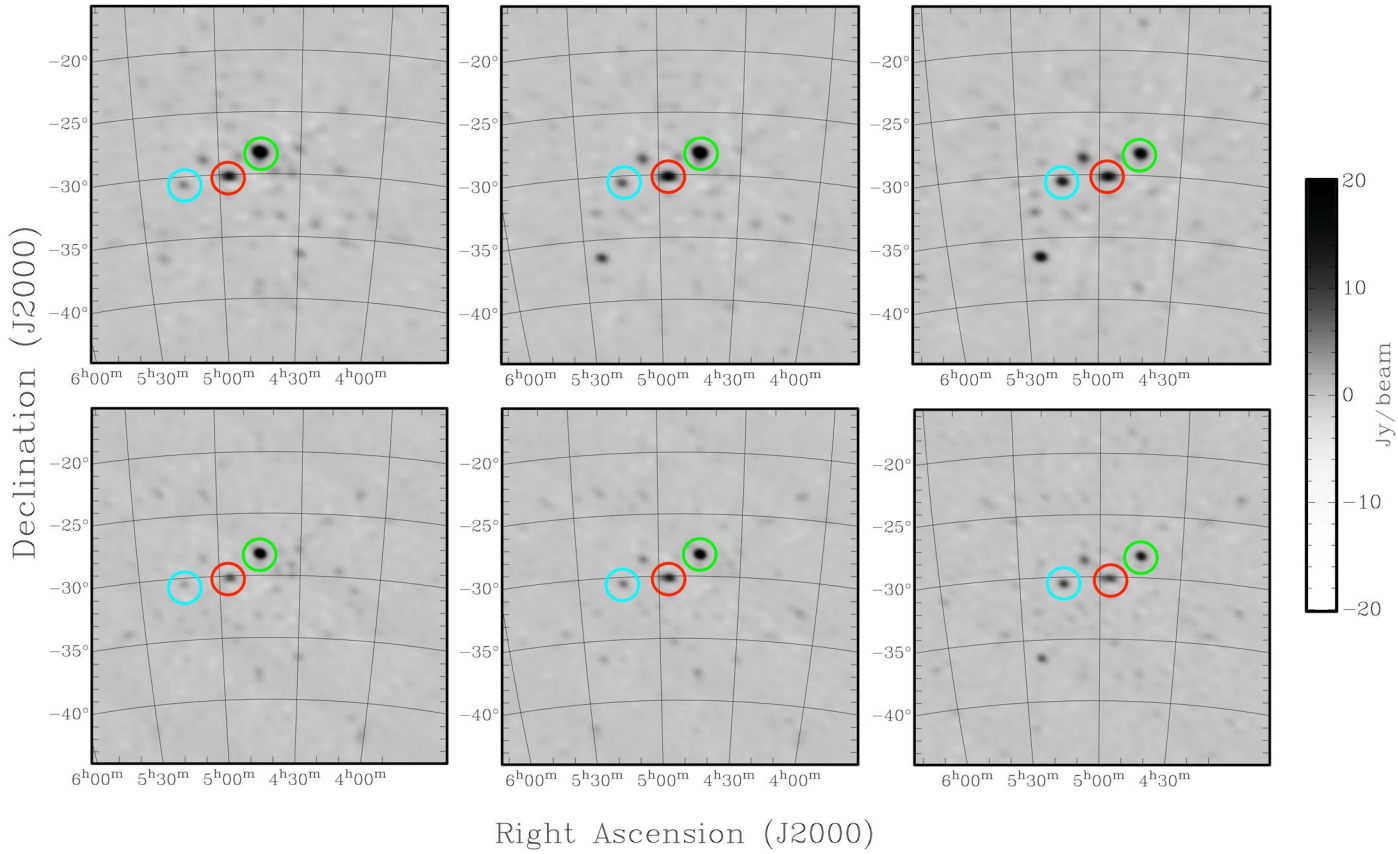

Figure 6. Snapshot images formed from the 10 MHz band centered at 130 MHz (top) and 150 MHz (bottom) for 3 consecutive 10 minute observations for the east–west polarizations. The three brightest sources in the snapshots are highlighted in red, blue, and green.

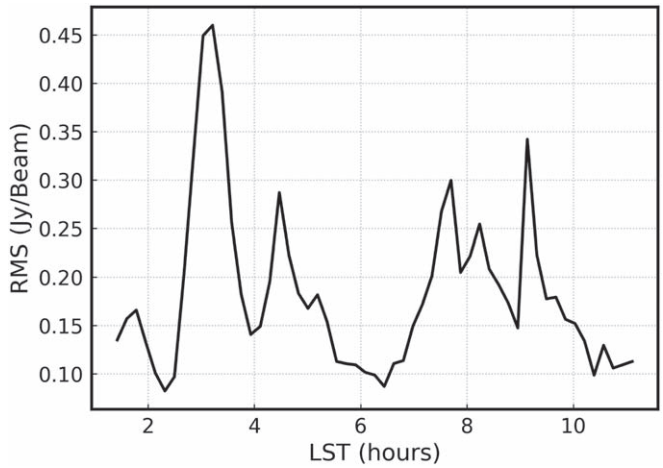

Figure 7. rms of the confusion background obtained by fitting a Gaussian profile to the flux density distribution in the images generated at different LSTs. The average rms is about 0.18 Jy, thus the threshold for source selection is chosen to be about five times the rms value.

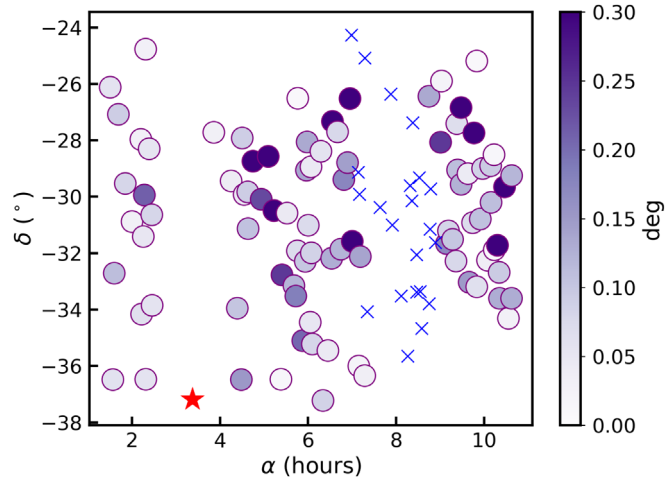

Figure 8. HERA sources found in the GLEAM survey are plotted in circles. Color indicates the absolute difference in angular position between the sources identified by PyBDSF and the matched candidates from the GLEAM survey. The blue crosses denote the sources that are not included in the GLEAM survey. The red star represents the brightest source in the FoV, Fornax A.

densities $I_\nu(\hat{s})$. We project the deconvolved images onto a HEALPIX grid (Górski et al. 2005) and the resulting maps are inputs to $I'_\nu(\hat{s}, t)$, and $A_\nu^M(\hat{s}, t)$ is calculated from the EM simulations. The top panel of Figure 9 depicts the 20° FoV of HERA. Our measurements are dominated by noise at the edges of and beyond the FoV, resulting in noisy $I_\nu(\hat{s})$. We highlight the source candidates identified by PYBDSF in yellow in the bottom panel of Figure 9. The brightest source, Fornax A, is circled in red.

Given the locations (right ascensions and declinations) of the source candidates, we extract their flux densities as follows. For a given source position (α, δ):

1. we select a region centered at the source location, with a radius equal to the synthesized beam.
2. we fit a Gaussian distribution to the selected region and evaluate the integrated flux density I'_ν. We prefer the

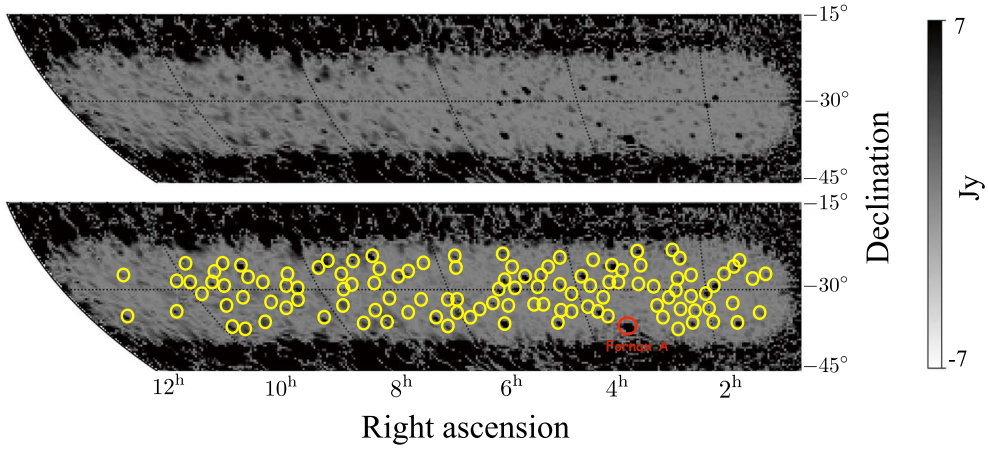

Figure 9. Top: a mosaic map formed from 10 minute observations spanning 12 hr in LST. Bottom: the same map with yellow circles marking the 112 potential source candidates identified by PyBDSF. The brightest source, Fornax A, is highlighted in red.

results of the Gaussian fit over PyBDSF outputs because of the gaps in our *uv* coverage resulting in the poor performance of PyBDSF.

3. we subtract the Gaussian distribution from the data and select a region, centered at the source location, with a radius equal to twice the synthesized beam. We then calculate the standard deviation of the selected region to obtain an estimate of the error $\Delta I_\nu'$ involved in the extraction process. The reason for choosing twice the synthesized beam for the error calculation is to include side-lobe contribution from nearby sources.

The measured flux densities of the three sources highlighted in Figure 6 at 150 MHz are plotted as a function of time in the left panel of Figure 10. We see that sources can be tracked down to confusion noise for about 6 hr, transiting the main lobe of the instrument for about 1.7 hr. The right panel shows the relative error associated with the measured flux values $\Delta I_\nu^{'}/I_\nu^{'}$, which increases as sources drift away from the main lobe due to the dominance of confusion noise in our measurements. The error within the main lobe, where we assume sufficient S/N, is plotted in the top-left inlet window. The error, on average, represented by the dotted blue lines, is found to be less than 10%.

The above analysis is conducted on 12 hr of data from 2018 December 24. In order to study day-to-day variations in the flux measurements, we repeated the aforementioned process on 12 hr of hours from 2018 December 25 to 26. The difference in flux measurements relative to these three consecutive days is shown in Figure 11. On average, the flux values vary by around 2%, but as the source moves away from zenith, we see that the difference increases up to 9%, consistent with the error associated with the flux extraction illustrated in Figure 10. It is worth noting that this error estimate might change if we increase the gap between days due to instrumental (e.g., system temperature) and atmospheric (e.g., ionosphere) effects.

3.4. Beam Construction

We apply the formalism derived in Section 2 to the 113 source tracks. The formalism is implemented in the `beam_solver`[24] (Nunhokee 2020) Python package. In this work, we mainly pursue the method of Pober et al. (2012) but our approach is slightly different. First, because HERA has two orthogonal dipoles as its feed, we use the 90° rotation between the east–west and north–south polarizations, illustrated in the bottom-left plot in Figure 1 in this work, similar to Eastwood et al. (2018) to break the degeneracy between source flux and beam response in our equations. The 90° rotation overcomes the issue of having a source track overlapping with the rotated one. However, given that we construct Equation (1) for each data point, certain data points might repeat themselves, thus including the same equations again in the system. We therefore discard such data points to avoid duplication. By using this 90° rotation, we inevitably reduce our beam solutions to a single polarization. Second, we work in the spatial or image domain to obtain our flux measurements whereas Pober et al. (2012) extracted the flux density using the delay transform approach (Parsons et al. 2012b). Working in the spatial domain allows flux densities per frequency to be extracted (discussed in Section 3.2), unlike the delay domain. Third, Pober et al. (2012) derived the beam solutions with only 25 sources followed by a deconvolution process to fill in the gaps. As the FWHM of HERA is about half that of PAPER, our measurements provide an entire beam coverage.

The rationale behind the framework presented in this paper is aimed at an ongoing series to know our averaged instrument response better. For instance, the synthesized beam generated by the CLEAN algorithm does not yield the nonidealities or small deviations on the primary beam. In order to derive these nonidealities, we need a system of equations as presented in Section 2, which includes a combination of the primary beams. Moreover, the redundantly calibrated visibilities used to derive the beam solutions were absolutely calibrated using two sources from GLEAM (refer to Section 3); therefore, the calibration solutions deliver limited information on the sources, while our beam-solving algorithm uses all the sources obtained from our observations to solve for the beam and source flux densities, which in turn enables us to measure small deviations from the primary beam.

The fit to the system of equations uses the flux density values estimated from Equation (4). We do not use the EM simulations but instead give zeros as input to the primary beam; however, we constrain the pixel corresponding to zenith to be unity. The beam solutions are sensitive to the grid size as mentioned in Section 2.1, hence choosing the proper grid size is important. We choose a grid size of 1° to conform to the

[24] https://github.com/Chuneeta/beam_solver

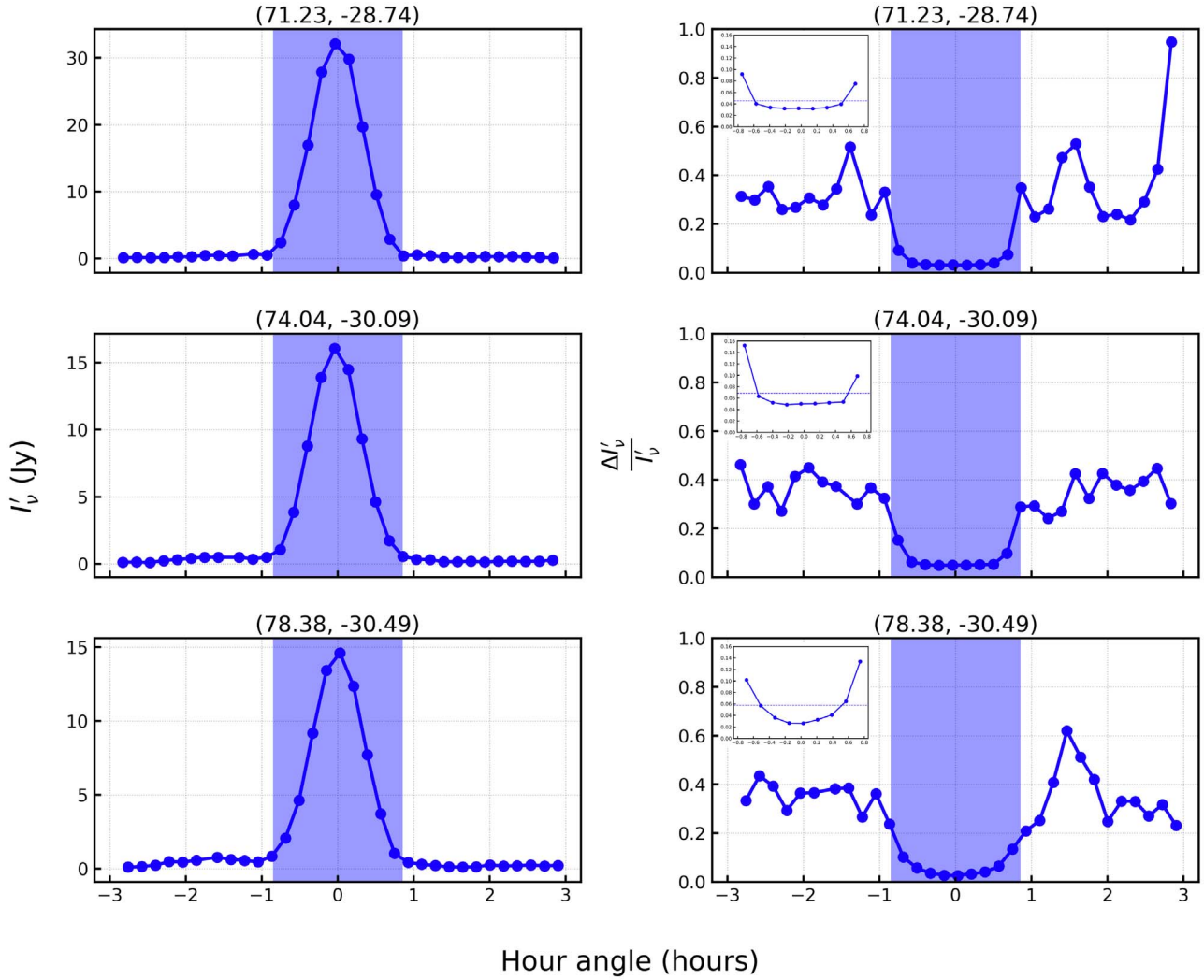

Figure 10. Left panel: flux densities of the sources marked in blue (top), red (middle), and green (bottom) in Figure 6 measured at 150 MHz. The shaded region indicates the time span of the source transiting the main lobe of the instrument's primary beam. Right panel: relative error associated with the measured flux densities. The inlet plot at the top-left corner shows a zoom version of the relative error for the source crossing the main lobe, and the dotted line represents the corresponding average relative error.

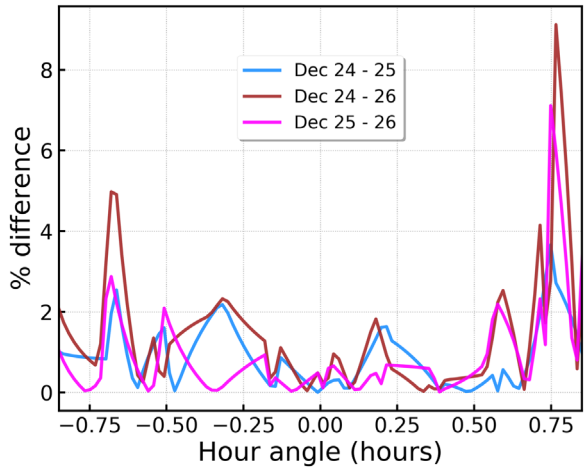

Figure 11. Difference in flux measurements between three consecutive days (2018 December 24, 25, and 26) relative to each other. The average difference between these three consecutive days is ∼2%.

assumptions on our beam symmetries. Given that we have a datum every 10 minutes, the same data point falls into multiple grids, resulting in additional degeneracies from poorly constrained pixels. We therefore interpolate between the data points every 3 minutes so that we have a unique datum for each grid. In order to estimate the uncertainties associated with the interpolated points, we require that the correlation between our flux measurements be understood. This derivation is analytically possible and will lead to a full correlation matrix referred to as the noise matrix $\boldsymbol{N}$ (see Section 4 for details). However, we adopt a partially correlated model instead to cut down the computational cost. This model assumes that each interpolated point is equally correlated between adjacent measurements and, as a result, leads to an overestimation of the uncertainties.

Even post-interpolation, some of the pixels remain poorly constrained. We therefore decomposed the condition matrix $\boldsymbol{C}$ from Equation (3) into its corresponding eigenvalues using singular value decomposition. An example of the output eigenamplitudes $|E_m|$ versus eigenmodes m is illustrated in Figure 12. We notice that after eigenmode 606, there is a drastic decrease in amplitude. The strange behaving eigenmodes reflect poorly constrained modes subject to numerical instability and noise, and projecting them out takes care of the degenerate modes. We discover that the amplitudes of the degenerate eigenmodes are about four orders of magnitude lower relative to the cumulative sum of $|E_m|$, hence we define

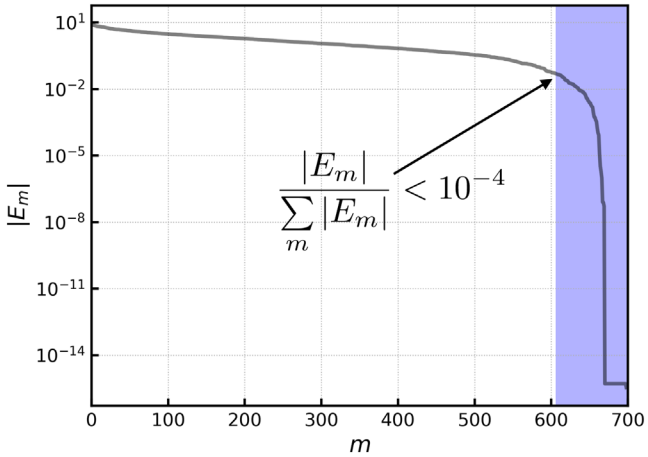

Figure 12. Eigenamplitude $|E_m|$ vs. eigenmodes m obtained by decomposing the condition $\boldsymbol{C}$. The shaded region marks the eigenmodes that are degenerate in the beam solutions.

the cutoff threshold such that all eigenmodes with $|E_m|/\sum_m |E_m| < 10^{-4}$ are discarded.

4. Beam Pattern Measurements

4.1. Initial Beam Solutions

The beam solutions derived at 150 MHz using the observations and following the processes described in Section 3 are shown in Figure 13. Given that the solutions are estimated from Equation (1), they represent the gain amplitude of the ratio of measured flux densities to the intrinsic or expected ones. The gain amplitude of an antenna, measured in units of decibels (dB) refers to the energy or power transmitted in the peak direction of the radiation relative to an isotropic source and is given by

$$G_{\rm dB} = 10 \log_{10} \left(\frac{A_\nu}{A_0} \right), \tag{8}$$

where A_0 is the reference energy (of isotropic source) and is equal to unity in our case.

The tracks formed by the beam solutions along the east–west and north–south directions demonstrate the 90° beam symmetry illustrated by the inset (refer to Sections 2 and 3.4). We obtain a circular-like beam, unlike the EM simulations that portray an elliptical shape (Figure 3); this is due to our measurements hitting the noise floor at or before the first null. We provide more evidence of the noise behavior in later sections.

Ideally, the beam solutions are expected to be symmetric about the center both along the east–west and north–south polarizations. We show a plot of the cut from Figure 13 through the zenith along the east–west polarization in the top panel of Figure 14. We see that the solutions within the main lobe, ∼10°, are almost symmetric about $\phi = 0°$; however, as the azimuth angle increases to 5°, the symmetry disappears. The solutions are scattered between −5° and −10°, and the gain amplitudes are higher, unlike those within 5° and 10°. The shaded region depicts errors on the beam solutions $\Delta G_{\rm dB}$, and they are calculated using $(\boldsymbol{C}\ \boldsymbol{N}^{-1}\ \boldsymbol{C}^{\boldsymbol{T}})^{-1}$, where $\boldsymbol{N}$ is a tridiagonal matrix containing errors evaluated during the

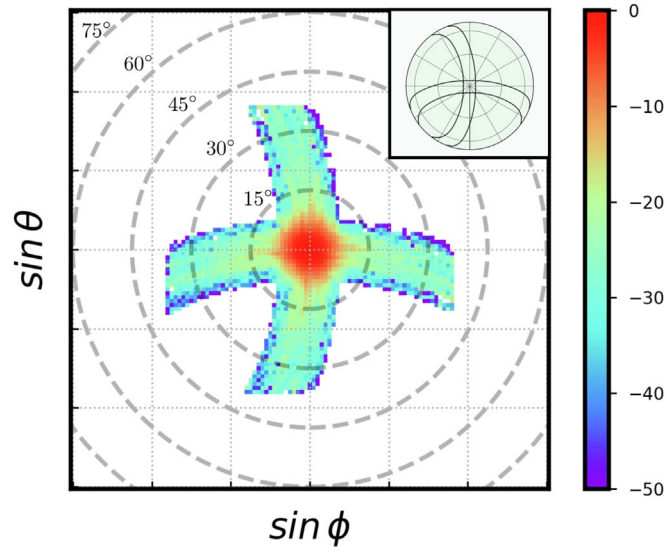

Figure 13. Beam solutions obtained using flux densities measured from images at 150 MHz. The inset shows the beam symmetry used to derive these beam solutions. The tails in the east–west and north–south directions with 10% gain amplitude relative to the peak gain throughout are suspected to be dominated by confusion noise. Therefore, to probe the actual beam response, we use measurements of known bright sources such as Pictor A, Virgo A, Hercules A, Centaurus A, and a few MRT sources (see Figures 17 and 18).

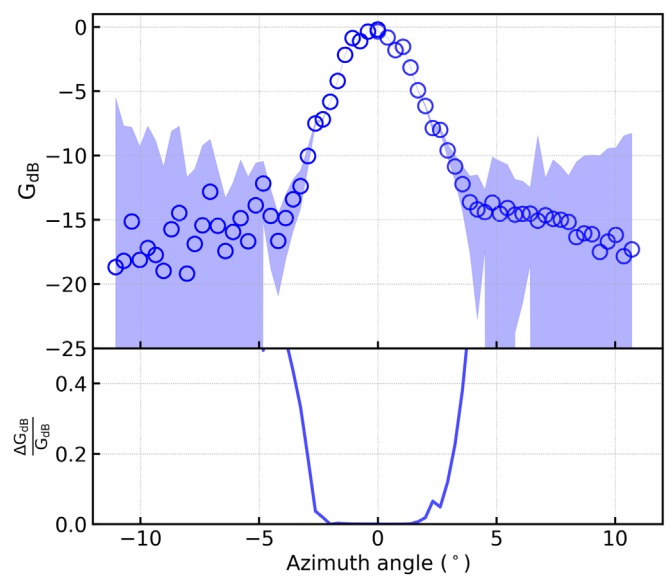

Figure 14. Top: beam solutions cut from Figure 13 representing the gain of our instrument across the east–west polarization, crossing through the zenith where it has the maximum sensitivity. Errors on the beam solutions $\Delta G_{\rm dB}$ are highlighted by the shaded region. Bottom: relative error with respect to the gain amplitude $\Delta G_{\rm dB}/G_{\rm dB}$, which is <5% within the main lobe and increases as it moves to the nulls.

interpolation (refer to Section 3.4). The relative error with respect to the gain amplitude $\Delta G_{\rm dB}/G_{\rm dB}$ plotted in the bottom panel is less than 5% within the main lobe and goes up to 40% in the side lobes. It is also observed that the errors for $\phi < -7°$ is higher than $\phi > 7°$. The cause for this behavior may be confusion noise in our measurements. Because sources with low S/N quickly drive down below noise level, we need

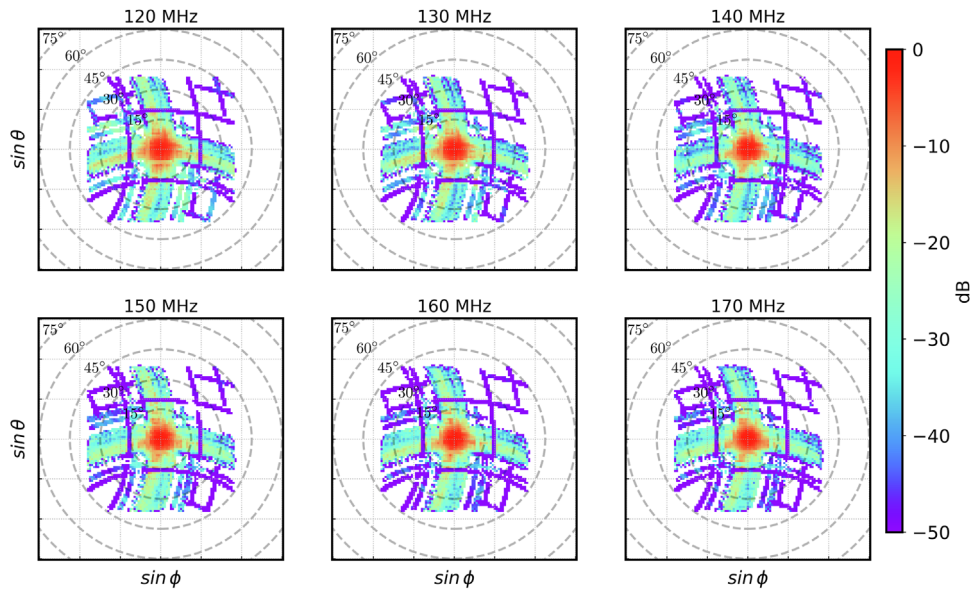

Figure 15. Beam solutions measured at various frequencies after including the bright sources. The additional tracks that we see here are the beam tracks constructed by these additional sources. The drop in amplitude confirms that the beam solutions in the tails are dominated by confusion noise.

measurements of a few bright sources to probe the actual beam response.

4.2. Improving Beam Solutions

Bright sources such as Pictor A, Virgo A, Hercules A, Centarus A, and a few candidates from the Mauritius Radio Telescope survey (MRT; Golap et al. 1998) are observed by HERA at noise level. We include these aforementioned sources in our least-squares optimization and constrain their corresponding intrinsic flux densities to be measurements from the literature. The flux densities of these bright sources are obtained from surveys carried out at 150 MHz (Israel 1998; Golap et al. 1998; Jacobs et al. 2013) and at 160 MHz (Slee 1995), and are scaled to the desired frequency using the power-law formula for synchrotron emission (Rybicki & Lightman 1986). Figure 15 displays the improved beam solutions derived at 120, 130, 140, 150, 160, and 170 MHz, plotted on a 2D grid. The isolated tracks represent the beam solutions formed by the additional bright sources. The amplitude drop in the solutions is about an order of magnitude, indicating that the beam response estimated beyond the main lobe is dominated by confusion noise in our data.

We characterize the spectral properties of the estimated beam solutions by tracing the beam response of the brightest source in our FoV, Fornax A, between the hour angles of −3 hr to 3 hr. The beam tracks regenerated using the improved solutions in Figure 15 at 120, 140, and 160 MHz are illustrated in the top panel of Figure 16. The maximum sensitivity of the regenerated beam responses at the various frequencies is centered at LST ∼0 hr, peaking at the same gain amplitude. We observe a decrease in FWHM with increasing frequency as the beam solid angle is inversely proportional to ν (Kraus 1986). Similar to Figure 14, the beam solutions between the hour angles of −3 hr and −2 hr have higher amplitude compared to those between hour angles of 2 hr and 3 hr. We speculated in Section 4.1 that this phenomenon may be due to confusion noise in our measurements. However, as our beam solutions are derived using a Fourier-transform implementation of the visibilities, they are basically tied to the gain solutions obtained

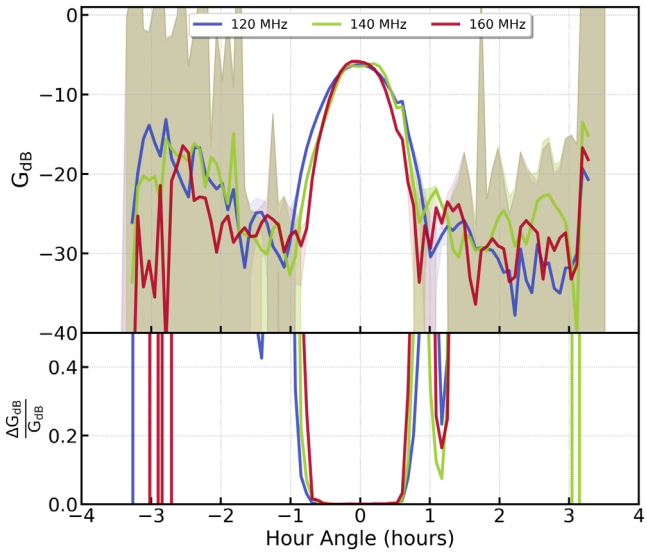

Figure 16. Top: regenerated tracks of Fornax A using the derived beam solutions in Figure 15 illustrating the changing FWHM with frequency. Shaded region indicates the error on the beam solutions. Bottom: error associated with the beam solutions relative to the gain amplitude, which shoots up to 40% beyond the main lobe.

from redundant calibration (Dillon et al. 2020), and the high S/N of Fornax A suggests possible calibration issues. The bottom plot shows the error relative to the gain of the beam amplitude, consistent with Figure 14.

4.3. Comparison with EM Simulations

In this section, we compare the beam solutions at 150 MHz with the EM simulations. To begin with, we regenerated the beam responses along the east–west polarization using the improved solutions at 150 MHz for the six brightest sources in the FoV. The regenerated beam responses are plotted in green in Figure 17. The position in degrees and strength in Jansky of the sources are displayed on top of each plot. The errors on the beam solutions $\Delta G_{\rm dM}$ are highlighted by the shaded green

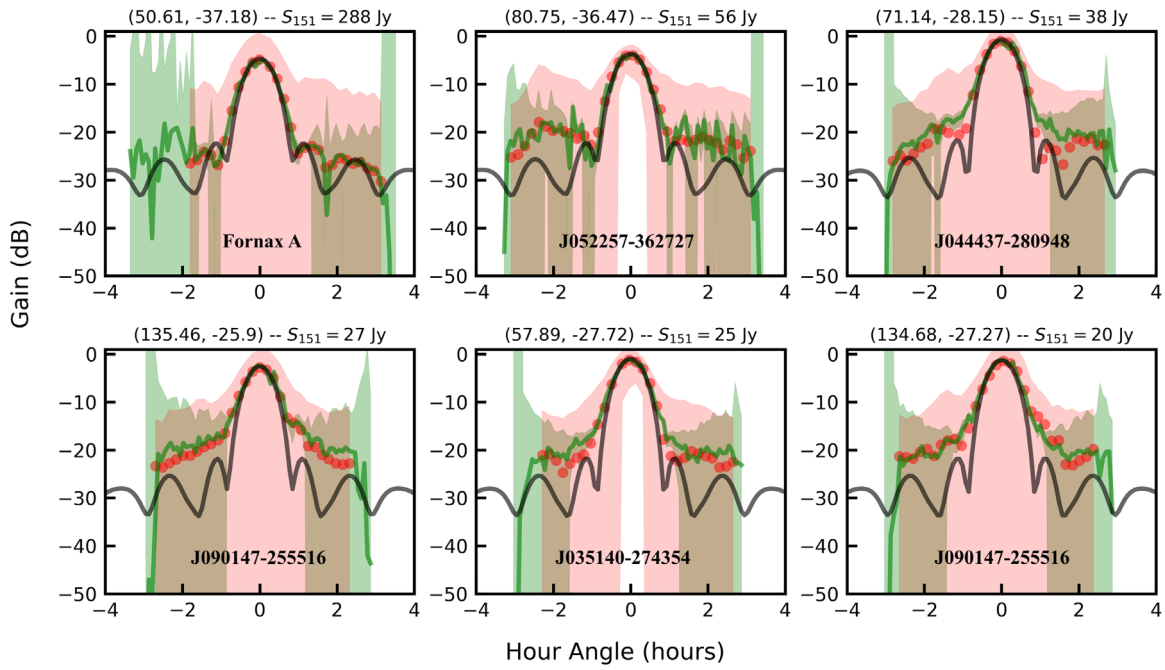

Figure 17. Gain amplitude defined in Equation (8) of the six brightest sources in our FoV evaluated from the beam solutions in Figure 15 (solid green line in top panel of each subplot) and EM simulations (black) at 150 MHz. The shaded region in green denotes the errors associated with the beam solutions. The ratio of the extracted flux densities $I_\nu(\hat{s}, t)$ to $I_\nu(\hat{s})$ calculated using Equation (4) are plotted in red. The shaded region in red highlights the 1σ errors on these flux measurements. The beam solutions follow our flux measurements down to the tails or side lobes and agree with EM simulations down to -20 dB.

region. They are consistent for all six sources and with Figure 14, increasing as the sources drift away from the main lobe.

The beam responses for the six brightest sources are symmetric about LST = 0 hr in the main lobe, consistent with Figures 14 and 15. The side lobes depict spiky features that might be fundamentally due to confusion noise as supported by the errors shaded in green; therefore, they are not reliable. Further, we do notice the large amplitude of the beam solutions observed in Fornax A between the hour angles of $\sim$3 and $\sim$2 hr in the remaining five sources. The evidence seems to be pointing toward the visibilities being less redundant when Fornax A enters the FoV (Dillon et al. 2020), and this requires further investigation that is beyond the scope of this work.

We then overplot the flux measurements in red on the beam solutions and find that they follow the desired source tracks, which is anticipated. The flux measurements plotted in Figure 17 are scaled such that they are equal to $I'_{150\mathrm{MHz}}(\hat{s}, t)/I_{150\mathrm{MHz}}(\hat{s}, t)$, where $I_{150\mathrm{MHz}}(\hat{s}, t)$ is obtained from Equation (4). The shaded region in red shows the 1σ errors associated with the flux measurements. The variations in the side lobes of the beam solutions are consistent with the errors on our flux measurements. Another thing to note here is that we do not have flux measurements for Fornax A for hour angles less than -2 hr unlike the remaining five sources, and this could be a potential cause for the high amplitude of the beam solutions and thus large error bars.

Next, we compare the beam solutions (green line) with the EM simulations plotted in black in Figure 17. The beam solutions matches the EM simulations down to about -20 dB relative to the peak amplitude. Moreover, with high S/N sources such as Fornax A, we could track the beam responses down to the first null as observed in the top-left panel of Figure 17. At the same time, we notice that the beam solutions beyond the main lobe for the other sources are about an order of magnitude higher than the EM simulations, which can be attributed to increasing confusion noise in the side lobes.

We repeat the aforementioned comparison for the six faintest sources, and the plots are illustrated in Figure 18. In this case, our measurements are able to go down to -10 dB only while the beam solutions in the main lobe goes down to -20 dB for most of the sources, apart from those displayed in the right panel. Beam solutions that go down to -20 dB seem to have fewer flux measurements (they are not fully tracked by our observations) as compared to those that go down to -10 dB, indicating that sources with high S/N are advantageous in improving our beam solutions. The discrepancies in our beam solutions are consistent for all the sources within 2σ. Note that the errors on the flux measurements (region shaded in red) shows the errors to 1σ.

The beam solutions in the main lobe agree down to about the -13 dB level relative to the peak gain with the EM solutions for the sources below 3 Jy. Similar to the bright sources, the beam solutions in the side lobes are an order of magnitude higher than the EM simulations for the non-fully tracked sources and are about two orders of magnitude brighter for the fully tracked sources. The measurements involved in deriving the beam solutions in the side lobes are mostly confusion noise; therefore, we expect the solutions to be highly contaminated by confusion noise.

We then rerun the least-squares optimization, but this time excluding the 22 sources that are located within the Magellanic Clouds and excluded in the GLEAM survey (refer to Section 3.3) to study the impact of these sources on our beam solutions. The resulting beam solutions do not show any variations for bright sources; however, slight distortions are seen in the fainter ones where confusion noise is the limiting factor. Because the brightest source among these excluded sources is about 31 Jy and the remaining ones are less than

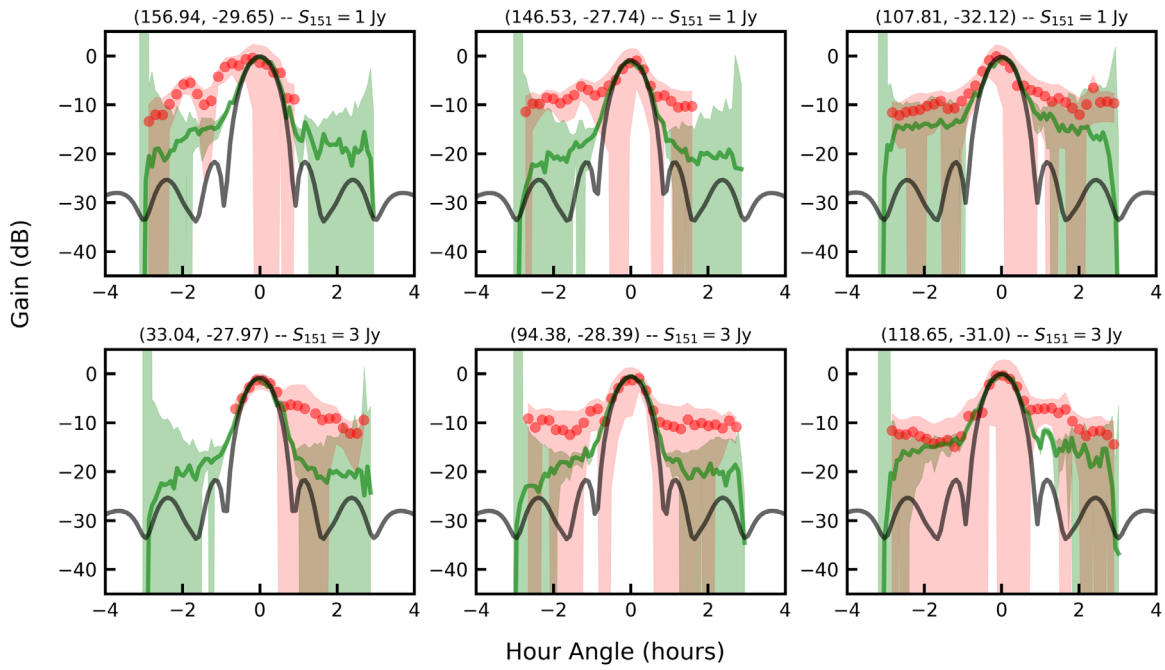

Figure 18. Same as Figure 17 but for the six faintest sources. Here we see that for most of the sources, our flux measurements are an order of magnitude higher than the beam solutions implying, that the least-squares optimization is driven by sources with high S/N. Our beam solutions match the EM simulations in the main lobe down to −13 dB. As we move away from the main lobe, our flux measurements hit the noise floor, thus the beam solutions are likely to be dominated by confusion noise.

15 Jy, we confirm that the beam solutions are sensitive to high S/N sources.

To further validate the beam solutions, we compare the FWHM of the beam solutions along the east–west polarization evaluated from Figure 15 with the EM simulations. The FWHM estimated for an arbitrary source transiting the zenith and the percentage difference relative to the EM simulations as a function of frequency are plotted in the top and bottom panels of Figure 19 respectively. We clearly see the decrease in FWHM with frequency as stated in Section 4.2, and our beam solutions agree with the EM simulations within less than 3%.

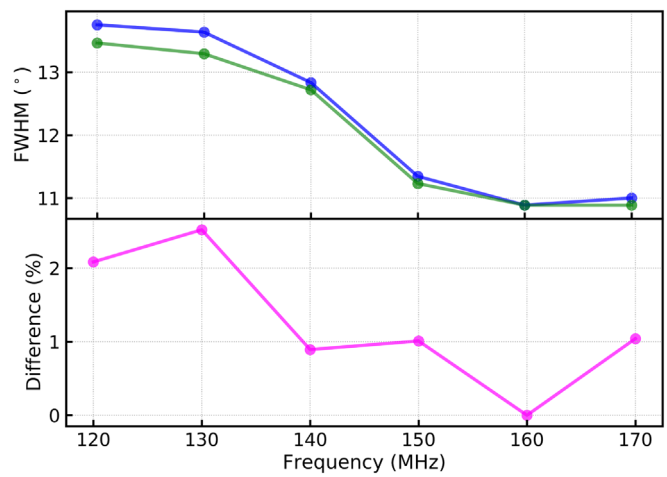

Figure 19. Top: FWHM evaluated using the beam solutions along the east–west polarization illustrated in Figure 15 (blue) and EM simulations (green) at various frequencies. Bottom: the percentage difference in FWHM relative to the EM simulations. We observe a good agreement between the beam solutions and EM simulations.

5. Source Catalog

We also estimate flux densities for the 113 sources that went into the least-squares optimization. We construct a source catalog displayed in Table 2 using these flux estimates. It covers an area of ∼3600 deg^2. We then compare the estimated flux densities with the GLEAM survey (Hurley-Walker et al. 2017) and find counterparts for 90 sources (refer to Figure 8). Sources in the GLEAM survey are resolved at an angular resolution of 2′ while our source measurements are resolved at 8′, revealing potential candidates being unresolved by HERA, unlike GLEAM measurements. For such sources, we add all the resolved GLEAM sources found within HERA's synthesized beam to match the flux density measured by HERA and use the position of the brightest source in the cluster to match the position of our sources. The measurements of these matched sources are reported in Table 2.

A description of the source catalog is as follows:

1. Column 1: source ID, taken from the GLEAM survey. If the flux density reported is the sum of multiple sources, ∗ is added at the end of the source ID corresponding to the brightest one in the cluster;
2. Column 2: right ascension (α) in degrees of the position measured by PyBDSF;
3. Column 3: right ascension (α_0) in degrees of the matched counterpart from the GLEAM survey;
4. Column 4: decl. (δ) in degrees of the position measured by PyBDSF;
5. Column 5: decl. (δ_0) in degrees of the matched counterpart from the GLEAM survey;
6. Column 6: estimated flux density at 151 MHz in Jy, S_{151};
7. Column 7: flux density of the matched source(s) measured by the GLEAM survey at 151 MHz, S_{G151}.

We examine the positional difference between our measurements and matched GLEAM counterpart, plotted in Figure 8,

Table 2
List of Sources Used in This Work and Their Derived Flux Densities

GLEAM ID	α (°)	α_0 (°)	δ (°)	δ_0 (°)	S_{151} (Jy)	S_{G151} (Jy)
J013027–260956	22.59	22.62	−26.12	−26.17	9.34 ± 2.40	11.76
J013411–362913	23.49	23.55	−36.48	−36.49	20.84 ± 2.42	18.55
J013527–324135*	23.97	23.86	−32.71	−32.69	3.14 ± 2.81	3.62
J015035–293158*	27.73	27.65	−29.53	−29.53	17.45 ± 3.52	17.75
J014127–270606	25.38	25.36	−27.08	−27.17	6.34 ± 2.79	8.0
J020012–305324	30.02	30.05	−30.88	−30.89	16.89 ± 4.41	17.95
J021209–280009	33.04	33.04	−27.97	−28.0	2.55 ± 1.30	2.61
J021317–341325*	33.3	33.32	−34.16	−34.22	6.0 ± 2.17	5.43
J021527–312144	33.87	33.86	−31.41	−31.36	3.62 ± 2.96	3.95
J021736–294750*	34.24	34.4	−29.94	−29.8	3.27 ± 1.94	3.19
J021843–244814	34.68	34.68	−24.77	−24.8	7.2 ± 2.84	8.97
J021902–362603	34.72	34.76	−36.47	−36.43	8.87 ± 3.59	9.36
J022343–281856	35.88	35.93	−28.3	−28.32	7.38 ± 4.39	7.81
J022720–303746	36.75	36.83	−30.64	−30.63	4.7 ± 1.66	4.96
J022716–335232	36.87	36.82	−33.85	−33.88	4.06 ± 2.52	5.11
J035140–274354*	57.89	57.92	−27.72	−27.73	25.19 ± 7.51	27.55
J041508–292901	63.79	63.79	−29.44	−29.48	8.04 ± 3.64	8.27
J042347–340234	65.9	65.95	−33.95	−34.04	4.54 ± 2.52	6.27
J042940–363050	67.27	67.42	−36.48	−36.51	13.81 ± 4.94	17.39
J043018–280045	67.58	67.57	−27.92	−28.01	5.23 ± 3.29	5.45
J043300–295609	68.21	68.25	−29.92	−29.94	5.55 ± 2.58	7.68
J043736–295359*	69.46	69.4	−29.83	−29.9	8.55 ± 4.10	8.02
J043832–311243*	69.57	69.64	−31.13	−31.21	5.22 ± 3.18	4.79
J044437–280948	71.23	71.16	−28.74	−28.16	37.7 ± 10.6	37.34
J045514–300646	74.04	73.81	−30.09	−30.11	16.95 ± 4.73	17.12
J050519–281628*	76.41	76.33	−28.57	−28.27	9.79 ± 4.15	10.34
J051135–301119*	78.38	77.9	−30.49	−30.19	15.42 ± 5.17	15.53
J052257–362727	80.75	80.74	−36.47	−36.46	55.7 ± 8.04	55.94
J052333–325119*	81.12	80.89	−32.77	−32.86	8.93 ± 4.21	9.57
J053115–303210	82.84	82.82	−30.58	−30.54	3.9 ± 2.32	4.22
J054017–330918	85.19	85.07	−33.15	−33.16	4.25 ± 2.95	4.78
J054358–333629*	85.83	85.99	−33.52	−33.61	4.21 ± 4.16	4.3
J054516–315853	86.36	86.32	−31.92	−31.98	3.56 ± 2.03	4.42
J054558–263015	86.49	86.49	−26.51	−26.5	4.39 ± 2.13	4.75
J055616–322310	87.57	89.07	−31.65	−32.39	7.1 ± 5.35	7.15
J055205–345955*	88.2	88.02	−35.1	−35.0	4.57 ± 2.01	4.65
J055616–322310	89.06	89.07	−32.29	−32.39	7.77 ± 3.53	7.15
J055759–285546	89.46	89.5	−29.06	−28.93	3.06 ± 1.79	3.44
J055820–280912	89.69	89.59	−28.06	−28.15	3.45 ± 2.34	4.46
J060015–305632*	90.08	90.06	−31.01	−30.94	8.78 ± 5.11	2.38
J060312–342632	90.75	90.8	−34.45	−34.44	8.38 ± 4.33	9.79
J060414–315555	91.12	91.06	−31.99	−31.93	8.45 ± 3.49	8.92
J060405–285843	91.0	91.02	−28.94	−28.98	3.11 ± 2.11	3.87
J060554–351806*	91.48	91.48	−35.22	−35.3	10.94 ± 4.78	10.23
J061721–282547	94.38	94.34	−28.39	−28.43	2.96 ± 1.56	4.98
J062000–371133	95.08	95.0	−37.22	−37.19	7.82 ± 4.19	9.83
J062707–352908	96.76	96.78	−35.45	−35.49	12.39 ± 4.26	16.58
J063433–271116	98.31	98.64	−27.33	−27.19	7.35 ± 3.56	7.64
J063149–321654	98.04	97.96	−32.18	−32.28	2.59 ± 1.65	3.36
J063957–274532	100.04	99.99	−27.7	−27.76	7.33 ± 3.21	6.13
J064413–315552	101.16	101.06	−31.86	−31.93	2.69 ± 1.74	3.0
J064925–291919*	102.19	102.35	−29.39	−29.32	3.33 ± 2.13	4.2
J065419–285218*	103.46	103.58	−28.79	−28.87	3.55 ± 1.54	3.58
J065818–263239*	104.28	104.58	−26.52	−26.54	4.99 ± 2.37	4.48
J065716–320328	105.06	104.32	−31.58	−32.06	3.43 ± 1.34	3.92
J071143–320300*	107.81	107.93	−32.12	−32.05	2.35 ± 1.19	2.48
J070901–355921*	107.28	107.26	−36.0	−35.99	5.59 ± 2.43	5.51
J071706–362140	109.31	109.28	−36.34	−36.36	8.42 ± 4.13	11.95
J084456–263332*	131.17	131.23	−26.44	−26.56	4.57 ± 2.12	5.53
J090147–255516	134.68	135.45	−27.27	−25.92	19.6 ± 4.22	31.35
J090015–281756*	135.15	135.06	−28.07	−28.3	5.43 ± 2.51	5.59
J090147–255516	135.46	135.45	−25.9	−25.92	26.72 ± 7.31	31.35
J090911–313334*	137.16	137.3	−31.66	−31.56	4.41 ± 2.36	5.53
J091123–310736*	137.83	137.85	−31.21	−31.13	4.85 ± 2.23	4.39

Table 2
(Continued)

GLEAM ID	α (°)	α_0 (°)	δ (°)	δ_0 (°)	S_{151} (Jy)	S_{G151} (Jy)
J091655–313637*	139.24	139.23	−31.51	−31.61	4.97 ± 2.13	4.66
J092121–321935*	140.4	140.34	−32.28	−32.33	4.95 ± 2.13	4.91
J092252–272627*	140.66	140.72	−27.41	−27.44	4.05 ± 2.11	3.98
J092410–290602*	140.94	141.04	−29.05	−29.1	5.58 ± 2.77	5.7
J092634–262355	142.12	141.64	−26.84	−26.4	3.62 ± 1.89	2.76
J092902–293017	142.15	142.26	−29.56	−29.5	5.8 ± 3.01	7.53
J093800–291244	144.12	144.5	−28.3	−29.21	11.67 ± 4.43	12.01
J093959–330710*	144.88	145.0	−33.03	−33.12	4.76 ± 2.34	3.42
J094401–305244*	146.06	146.0	−30.92	−30.88	3.3 ± 1.51	3.26
J094649–272049*	146.53	146.71	−27.74	−27.35	2.04 ± 1.43	1.95
J095003–330824	147.47	147.51	−33.19	−33.14	4.08 ± 1.90	4.2
J094953–251138	147.48	147.47	−25.19	−25.19	5.31 ± 4.21	11.47
J095433–305326*	148.68	148.64	−30.79	−30.89	6.51 ± 3.21	6.65
J095804–290408*	149.47	149.52	−29.0	−29.07	8.44 ± 5.2	8.26
J100439–321639	151.14	151.16	−32.25	−32.28	4.72 ± 2.3	5.03
J100910–285552	152.2	152.29	−28.9	−28.93	5.13 ± 2.35	5.7
J100855–301114*	152.34	152.23	−30.2	−30.19	5.09 ± 3.11	5.01
J101329–283118	153.36	153.37	−28.51	−28.52	5.76 ± 2.34	5.73
J101348–315323	153.45	153.45	−31.88	−31.89	5.84 ± 2.87	7.14
J102056–321100*	154.52	155.24	−31.72	−32.18	5.97 ± 2.56	5.21
J102011–324533	155.1	155.05	−32.68	−32.76	7.13 ± 3.56	8.95
J102020–333556*	155.22	155.09	−33.6	−33.6	6.12 ± 3.29	6.0
J102633–294054*	156.94	156.64	−29.65	−29.68	1.44 ± 1.04	1.62
J103312–341842	158.27	158.3	−34.31	−34.31	7.26 ± 3.67	12.12
J103704–334313*	159.32	159.27	−33.6	−33.72	7.25 ± 4.21	5.8
J103723–290749	159.36	159.35	−29.25	−29.13	4.37 ± 2.13	3.57

and find that sources that expose an absolute positional difference of about 30% are resolved by the GLEAM survey. Because (α_0, δ_0) for such sources correspond to the position of the brightest source in the cluster, slight phase shifts can be expected.

Figure 20 shows the flux densities of the GLEAM counterparts versus our flux density estimates. Our results are consistent with the GLEAM measurements within the estimated errors, except for a few sources ("J061721–282547," "J094953–251138," and "J103312–341842"). To further study the discrepant behavior of these sources, we plotted the ratio of our flux density estimates to GLEAM measurements in Figure 21. We observe no obvious correlation with the ratios and source positions. The ratio for these sources goes up to 1.5; therefore, the difference in telescope resolution cannot be blamed. This discrepant behavior may be due to errors involved in the calibration process that are more pronounced in off-zenith sources.

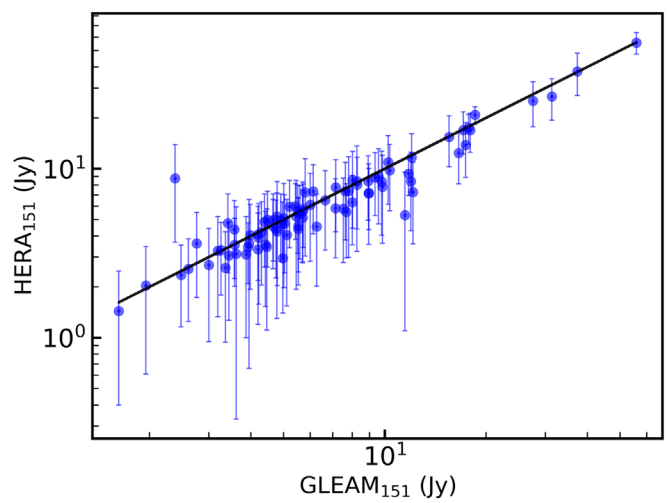

Figure 20. Flux densities of the 90 matching components from GLEAM S_{G151} plotted against the derived flux densities S_{151} reported in Table 2. Most of our flux measurements align with the GLEAM results within the quoted errors except a few, namely "J061721–282547," "J094953–251138," and "J103312–341842."

6. Effects of Confusion Noise

In this section, we investigate the effects of confusion noise on our results and test the robustness of our method. For each time sample and frequency channel, we perform the following operations:

1. Generate the sky emission, evaluating Equation (1) where the sky model consists of a catalog of point sources. The primary beam response A_ν is calculated from EM simulations.
2. Simulate visibilities via a discrete Fourier transform (Thompson et al. 2017) using the tools available in CASA.
3. Form images and extract the flux densities of sources as per Sections 3.2 and 3.3, respectively.
4. Construct a nonlinear least-squares problem (Section 2) and solve for the beam solutions and flux densities as described in Section 3.4.
5. Repeat steps (1) to (4) adding Gaussian noise to the sky emission. The rms is taken to be about 10% of the peak amplitude of the source.

We first use a single 1 Jy point source catalog and carry out the simulations. We are able to fully recover the input flux

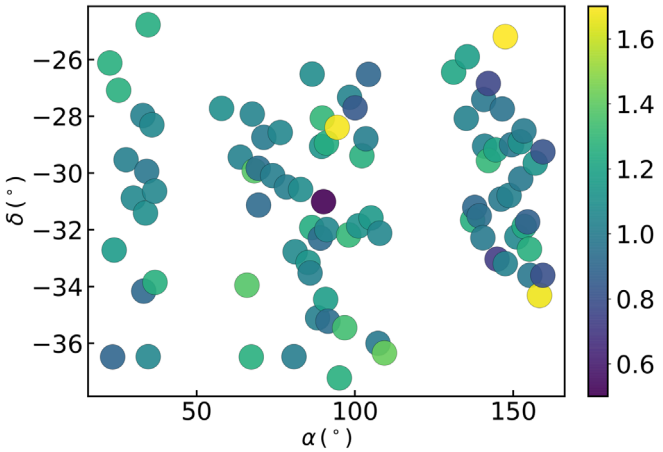

Figure 21. Scatter plot of the R.A. vs. decl. of the matching sources to examine trends in our flux densities vs. source locations. The color of each source indicates the ratio of the derived flux densities to those of the matching GLEAM component. We found no correlation between the flux densities and the source locations. The three discrepant sources seen in Figure 20 depict ratios >1.5.

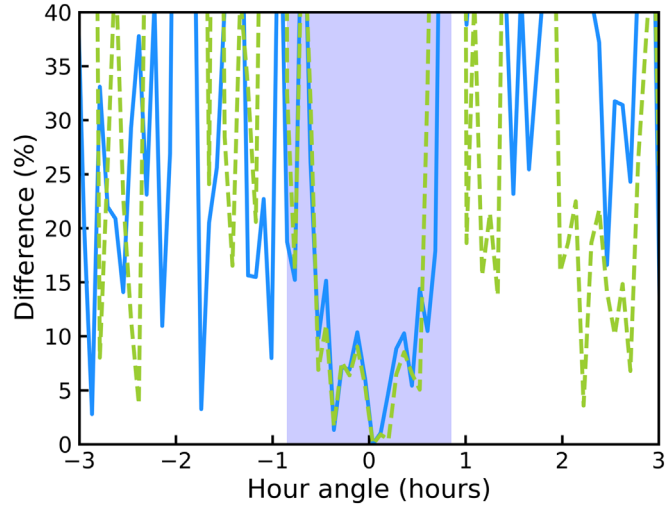

Figure 22. Simulations demonstrating that confusion noise is the dominant systematics in our approach. Adding Gaussian noise to our simulations yields negligible change inside the main lobe. We plot the percentage difference between the input and recovered beam of a transiting arbitrary source evaluated from a noiseless simulation, in blue. We added Gaussian noise to the simulations, and the resulting difference is plotted in green. The shaded area represents the main lobe of the beam response.

density and beam responses in both the noisy and noiseless cases, showing that thermal noise has no significant effect on our results. With a single source, we have no confusion noise and therefore it validates our formalism.

The simulation is then extended to the source catalog comprising 113 sources derived in Section 5. We regenerate the source tracks for an arbitrary source from the beam solutions obtained using the noiseless simulations. We calculate the difference between the EM simulations and the regenerated source tracks, illustrated in blue in Figure 22. The errors in the simulated beam solutions in the main lobe (shaded region) are <15% and increases up to 40% in the side lobes. This behavior is consistent with our measurements shown in Figures 17 and 18. The errors highlighted here indicates a combination of the errors associated with the flux extraction (Figure 10) and the errors in the beam formalism (Figure 19).

Including Gaussian noise in the sky emission does not induce major changes (green; Figure 22) within the main lobe. Nevertheless, the difference varies outside the main lobe. The difference seems to be smaller for some hour angles and higher for others compared to the noiseless case. Because the confusion noise becomes significant beyond the main lobe, the average between thermal noise and confusion noise may trigger these fluctuations.

7. Conclusions

We have presented a technique to measure the empirical beam pattern using wide-field drift-scan observations from HERA. The technique is driven by the ability of our instrument to track the flux density of sources in the FoV as they pass overhead. We formed snapshot images from a 10 MHz band centered at 120, 130, 140, 150, 160, and 170 MHz using 10 minute observations from HERA Phase I, exposing 113 sources in the FoV. We measured the flux densities of these sources from the images and built a nonlinear least-squares problem. We formed a network of overlapping sources using a 90° rotation about the east–west polarization (lower-right panel of Figure 1) to represent the beam response in the north–south polarization. This beam symmetry breaks the degeneracy between flux density and beam solution in the least-squares optimization.

The aim of the formalism derived in this paper is to measure small deviations present in our primary beam without the need for precise knowledge of the sky. It uses a least-squares approximation that allows the primary beam and flux values to be solved simultaneously. The system requires the initial inputs to the flux densities and beam solutions to converge.

The amplitudes of our initial beam solutions in the side lobes are about 10% relative to the peak in the main lobe. We therefore included some known bright sources observed at the noise level by HERA to probe the actual beam response in our least-squares optimization. The beam tracks formed by these additional sources reveal confusion noise in the side lobes, affirming that we should not rely on the beam solutions beyond the main lobe.

We further used our beam solutions to generate the beam responses of the six brightest and faintest sources in the FoV. Our beam estimates match the EM simulations in the main lobe down to a −20 dB and −13 dB level relative to the peak gain for sources with high and low S/N, respectively. They are one to two orders of magnitude higher in the side lobes. This behavior is caused by confusion noise in our flux measurements and therefore cannot be trusted as stated in the paragraph above. Our results demonstrate that the elements in the array are illuminated well by the feeds in the main lobe with sensitivity levels consistent with the EM simulations.

When evaluating the 21 cm H1 power spectrum (Parsons et al. 2012a), the power is required to be normalized by the power-squared beam of the observing instrument (see Appendix of Parsons et al. 2012a). Because our beam solutions are less noise dominated for high-S/N sources, we made a conservative estimate of this power-squared beam using the beam solutions for the six brightest sources. When compared with EM simulations, the difference is about ∼5%, which may be significant enough to contaminate the cosmological signal. However, our measurements are prone to confusion noise and calibration errors; therefore, improving on our instrument's

sensitivity and calibration methodologies should improve our beam measurements.

We also generated a catalog of 113 sources at 151 MHz covering an area of $\sim$3600 deg^2 from the flux densities estimated in the least-squares optimization. The flux density estimates agree with the measurements from the GLEAM survey (Hurley-Walker et al. 2017) within 10%–15%, except for a few sources. These discrepancies might be due to calibration errors; however, further investigation is required that is beyond the sphere of this work.

Additionally, we carried out simulations to test the accuracy of our technique and at the same time study the impact of confusion noise on our observations. We used the EM simulations as our primary beam response to the sky emission. The beam solutions seem to agree with the EM solutions within $<$15% within the main lobe. This error incorporates the error involved in the extraction process as well, which is about 10%, indicating that our least-squares approximate implementation is accurate down to about 5%. We also found that thermal noise has a negligible influence on our beam solutions inside the main lobe.

This work can be extended to include mutual coupling between neighboring antennas. We excluded this effect in this paper as our observations were calibrated using EM simulations excluding mutual coupling. Moreover, we assumed that all elements in the array have the same beam response throughout this work, which does not hold in practice. The variations in beam responses from antenna to antenna contribute to modeling errors in calibration, particularly for wide-field observations, and this may result in significant contaminations of the cosmological signal.

This material is based upon work supported by the National Science Foundation under grant Nos. 1636646 and 1836019, and institutional support from the HERA collaboration partners. This research is funded in part by the Gordon and Betty Moore Foundation. Parts of this research were supported by the Australian Research Council Centre of Excellence for All Sky Astrophysics in 3 Dimensions (ASTRO 3D), through project number CE170100013. HERA is hosted by the South African Radio Astronomy Observatory, which is a facility of the National Research Foundation, an agency of the Department of Science and Innovation. G.B. acknowledges funding from the INAF PRIN-SKA 2017 project 1.05.01.88.04 (FORE–CaST), support from the Ministero degli Affari Esteri della Cooperazione Internazionale-Direzione Generale per la Promozione del Sistema Paese Progetto di Grande Rilevanza ZA18GR02, and the National Research Foundation of South Africa (grant No. 113121) as part of the ISARP RADIO-SKY2020 Joint Research Scheme, from the Royal Society and the Newton Fund under grant NA150184, and from the National Research Foundation of South Africa (grant No. 103424).

ORCID iDs

Chuneeta D. Nunhokee https://orcid.org/0000-0002-5445-6586
Nicholas S. Kern https://orcid.org/0000-0002-8211-1892
Jonathan C. Pober https://orcid.org/0000-0002-3492-0433
Gianni Bernardi https://orcid.org/0000-0002-0916-7443
Chris L. Carilli https://orcid.org/0000-0001-6647-3861
James E. Aguirre https://orcid.org/0000-0002-4810-666X
Adam P. Beardsley https://orcid.org/0000-0001-9428-8233
Judd D. Bowman https://orcid.org/0000-0002-8475-2036
Joshua S. Dillon https://orcid.org/0000-0003-3336-9958
Aaron Ewall-Wice https://orcid.org/0000-0002-0086-7363
Steve R. Furlanetto https://orcid.org/0000-0002-0658-1243
Bryna J. Hazelton https://orcid.org/0000-0001-7532-645X
Daniel C. Jacobs https://orcid.org/0000-0002-0917-2269
Joshua Kerrigan https://orcid.org/0000-0002-1876-272X
Piyanat Kittiwisit https://orcid.org/0000-0003-0953-313X
Saul A. Kohn https://orcid.org/0000-0001-6744-5328
Matthew Kolopanis https://orcid.org/0000-0002-2950-2974
Paul La Plante https://orcid.org/0000-0002-4693-0102
Adrian Liu https://orcid.org/0000-0001-6876-0928
Miguel F. Morales https://orcid.org/0000-0001-7694-4030
Abraham R. Neben https://orcid.org/0000-0001-7776-7240
Nipanjana Patra https://orcid.org/0000-0002-9457-1941
Nithyanandan Thyagarajan https://orcid.org/0000-0003-1602-7868
Peter K. G. Williams https://orcid.org/0000-0003-3734-3587

References

Bandura, K., Addison, G. E., Amiri, M., et al. 2014, Proc. SPIE, 9145, 914522
Berger, P., Newburgh, L. B., Amiri, M., et al. 2016, Proc. SPIE, 9906, 99060D
Bernardi, G., de Bruyn, A. G., Harker, G., et al. 2010, A&A, 522, A67
Bernardi, G., Greenhill, L. J., Mitchell, D. A., et al. 2013, ApJ, 771, 105
Bowman, J. D., Morales, M. F., & Hewitt, J. N. 2009, ApJ, 695, 183
Chapman, E., Zaroubi, S., Abdalla, F. B., et al. 2016, MNRAS, 458, 2928
Ciardi, B., & Ferrara, A. 2005, SSRv, 116, 625
Cornwell, T. J., Golap, K., & Bhatnagar, S. 2005, in ASP Conf. Ser. 347, ADASS XIV, ed. P. Shopbell, M. Britton, & R. Ebert (San Francisco, CA: ASP), 86
de Lera Acedo, E., Bolli, P., Paonessa, F., et al. 2018, ExA, 45, 1
DeBoer, D. R., Parsons, A. R., Aguirre, J. E., et al. 2017, PASP, 129, 045001
Dillon, J. S., Kohn, S. A., Parsons, A. R., et al. 2018, MNRAS, 477, 5670
Dillon, J. S., Lee, M., Ali, Z. S., et al. 2020, arXiv:2003.08399
Dillon, J. S., & Parsons, A. R. 2016, ApJ, 826, 181
Eastwood, M. W., Anderson, M. M., Monroe, R. M., et al. 2018, AJ, 156, 32
Fagnoni, N., de Lera Acedo, E., DeBoer, D. R., et al. 2019, arXiv:1908.02383
Furlanetto, S. R. 2016, in Understanding the Epoch of Cosmic Reionization, ed. A. Mesinger (Cham: Springer), 247
Golap, K., Shankar, N. U., Sachdev, S., Dodson, R., & Sastry, C. V. 1998, JApA, 19, 35
Górski, K. M., Hivon, E., Banday, A. J., et al. 2005, ApJ, 622, 759
Hurley-Walker, N., Callingham, J. R., Hancock, P. J., et al. 2017, MNRAS, 464, 1146
Israel, F. P. 1998, A&Ar, 8, 237
Jacobs, D. C., Burba, J., Bowman, J. D., et al. 2017, PASP, 129, 035002
Jacobs, D. C., Parsons, A. R., Aguirre, J. E., et al. 2013, ApJ, 776, 108
Kern, N. S., Dillon, J. S., Parsons, A. R., et al. 2020, ApJ, 890, 122
Kerrigan, J., la Plante, P., Kohn, S., et al. 2019, MNRAS, 488, 2605
Kerrigan, J. R., Pober, J. C., Ali, Z. S., et al. 2018, ApJ, 864, 131
Koopmans, L., Pritchard, J., Mellema, G., et al. 2015, in Proc. Advancing Astrophysics with the Square Kilometre Array (AASKA14) (Trieste: SISSA), 1
Kraus, J. D., Tiuri, M., Raisanen, A. V., & Carr, T. D. 1986, Radio Astronomy Receivers (Powell, OH: Cygnus-Quasar Books)
Line, J. L. B., McKinley, B., Rasti, J., et al. 2018, PASA, 35, 45
Liu, A., Parsons, A. R., & Trott, C. M. 2014a, PhRvD, 90, 023018
Liu, A., Parsons, A. R., & Trott, C. M. 2014b, PhRvD, 90, 023019
Liu, A., Tegmark, M., Bowman, J., Hewitt, J., & Zaldarriaga, M. 2009, MNRAS, 398, 401
Liu, A., Tegmark, M., Morrison, S., Lutomirski, A., & Zaldarriaga, M. 2010, MNRAS, 408, 1029
McMullin, J. P., Waters, B., Schiebel, D., Young, W., & Golap, K. 2007, in ASP Conf. Ser. 376, Astronomical Data Analysis Software and Systems XVI, ed. R. A. Shaw, F. Hill, & D. J. Bell (San Francisco, CA: ASP), 127
McQuinn, M. 2016, ARA&A, 54, 313
Mitchell, D. A., Greenhill, L. J., Wayth, R. B., et al. 2008, ISTSP, 2, 707

Mohan, N., & Rafferty, D. 2015, PyBDSF: Python Blob Detection and Source Finder, Astrophysics Source Code Library, ascl:1502.007
Morales, M. F., Bowman, J. D., & Hewitt, J. N. 2006, ApJ, 648, 767
Morales, M. F., & Hewitt, J. 2004, ApJ, 615, 7
Neben, A. R., Bradley, R. F., Hewitt, J. N., et al. 2016, ApJ, 826, 199
Newburgh, L. B., Bandura, K., Bucher, M. A., et al. 2016, Proc. SPIE, 9906, 99065X
Nunhokee, C. 2020, Beam Solver: Solving for empirical primary beam using drift-scan radio interferometric observations, v1.0.0, Zenodo, doi:10.5281/zenodo.3755251
Nunhokee, C. D., Bernardi, G., Kohn, S. A., et al. 2017, ApJ, 848, 47
Paciga, G., Chang, T.-C., Gupta, Y., et al. 2011, MNRAS, 413, 1174
Parsons, A., Pober, J., McQuinn, M., Jacobs, D., & Aguirre, J. 2012a, ApJ, 753, 81
Parsons, A. R., Backer, D. C., Foster, G. S., et al. 2010, AJ, 139, 1468
Parsons, A. R., Pober, J. C., Aguirre, J. E., et al. 2012b, ApJ, 756, 165
Pober, J. C., Parsons, A. R., Aguirre, J. E., et al. 2013, ApJL, 768, L36
Pober, J. C., Parsons, A. R., Jacobs, D. C., et al. 2012, AJ, 143, 53
Procopio, P., Wayth, R. B., Line, J., et al. 2017, PASA, 34, e033
Pupillo, G., Naldi, G., Bianchi, G., et al. 2015, ExA, 39, 405
Rybicki, G. B., & Lightman, A. P. 1986, Radiative Processes in Astrophysics (Oxford: Wiley), 400
Slee, O. B. 1995, AuJPh, 48, 143
Thompson, A. R., Moran, J. M., & Swenson, G. W. J. 2017, Interferometry and Synthesis in Radio Astronomy (3rd ed.; Berlin: Springer)
Thyagarajan, N., Jacobs, D. C., Bowman, J. D., et al. 2015a, ApJL, 807, L28
Thyagarajan, N., Jacobs, D. C., Bowman, J. D., et al. 2015b, ApJ, 804, 14
Tingay, S. J., Goeke, R., Bowman, J. D., et al. 2013, PASA, 30, e007
van Haarlem, M. P., Wise, M. W., Gunst, A. W., et al. 2013, A&A, 556, A2
Vedantham, H., Udaya Shankar, N., & Subrahmanyan, R. 2012, ApJ, 745, 176
Virone, G., Paonessa, F., Peverini, O. A., et al. 2014, IAWPL, 13, 169
Yatawatta, S., de Bruyn, A. G., Brentjens, M. A., et al. 2013, A&A, 550, A136
Zaroubi, S. 2013, The First Galaxies, ed. T. Wiklind, B. Mobasher, & V. Bromm, Vol. 396 (Berlin: Springer), 45
Zheng, H. 2014, AAS Meeting, 224, 318.07